POLITECNICO DI TORINO

Master's Degree in Mechatronic Engineering

Master's Degree Thesis

DESIGN AND CONTROL OF AN EXPERIMENTAL TEST SYSTEM FOR A LINEAR ELECTRODYNAMIC LEVITATION DEVICE

Supervisors

Prof. Nicola AMATI

Prof. Andrea TONOLI

Dr. Renato GALLUZZI

Dr. Salvatore CIRCOSTA

Candidate

Federica FANIGLIULO

A.Y. 2020/2021

Abstract

The increasing need for a fast, efficient, and environmentally sustainable transportation paradigm has pushed growing interest towards the class of magnetic levitation trains. In this scenario, the *Hyperloop* concept has been subject to special attention, given its capability of reaching ultra-high speeds (up to 1200km/h). However, the feasibility of this technology is entangled to the stability of its electrodynamic levitation system. State of the art literature provides a method for accurate modelling of the coupling between the electrical and mechanical domains in the Linear Time Invariant systems framework: this technique allows to easily identify the unstable behaviour of the device and remove it by introducing additional damping through a secondary suspension. The purpose of this thesis consists in discussing the main steps that led to the design of a test bench for a *Hyperloop*-like levitation device, to validate the results of the above described approach. After a brief literature review, the main features of the experiment, relevant physical variables and their measurement systems are introduced and motivated. After having found a scale factor that suits the maximum allowable dimensions, actuator limitations and measurement feasibility, suspension design and control are addressed. At first, the damping that optimises stability is identified, and upon its value a suitable suspension architecture is discussed. In particular, the use of a voice coil actuator as a damper is motivated, and several linear control algorithms are compared and implemented, both in the modelling and in the software framework: processor-in-the-loop and hardware-in-the-loop tests provide feasibility analysis on the physical implementation of the proposed stabilisation strategies.

Acknowledgements

Ai miei genitori e a mia sorella,
le mie stelle Polari.
Ad Alessandro, Andrea, Arianna e Chiara,
la loro vicinanza è stata fondamentale.

I would like to express my gratitude to Professors Nicola Amati and Andrea Tonoli, for having provided me with this challenging yet amazing opportunity. Furthermore, I am very thankful to Dr. Salvatore Circosta and Dr. Renato Galluzzi who, with patience, have been guiding my work since the first day, and to my colleague and friend Alessia D'Oronzo, with whom I shared the latest months working on this project.

A special mention goes for Dr. Torbjorn Lembke from Hyperloop Transportation Technologies, for his precious feedback.

Finally, a huge shout-out goes to my friends, with whom I share memories of the best five years of my life, and to the city of Turin itself, which enchanted me with its elegance and pride.

Table of Contents

List of Tables

List of Figures

Acronyms

MCU
: micro-controller unit

EDB
: electro-dynamic bearings

PM
: permanent magnet

FEM
: finite element modelling

DOF
: degrees of freedom

HTT
: *Hyperloop Transportation Technologies*

LTI
: linear time invariant

OFE
: oxigen-free electronic

VCA
: voice coil actuator

MIL
: model in the loop

SIL

software in the loop

PIL

processor in the loop

Chapter 1

Introduction

This thesis aims at illustrating the design an implementation of an experiment whose purpose is to test a scaled version of a Hyperloop-like levitation system. It is the result of cooperation between professors and researchers at the *Mechatronics Lab* at Politecnico di Torino and the US company *Hyperloop Transportation Technologies*. After having introduced the framework in which the research has been carried out, a brief literature review and detailed thesis goal and outline are discussed.

1.1 Levitation-based transport systems

Recent events have dramatically increased people's awareness on the climate crisis; in this regard, scientists and engineers are encouraged in developing projects aimed at reducing the environmental impact of mankind on the planet. In this regard, transport is one of the most challenging issues, given the need to cope with both sustainability and the increasing urge to travel either on business or on vacation: furthermore, this course of action finds support from ruling classes all over the world through dedicated fundings aimed at pursuing innovation in this field [1, 2]. The future of transportation lies most likely in fast, reliable and yet low emission frameworks, and one of the most efficient solutions is that of magnetic levitation based systems. Such technology features, in general, suspension of an item without any additional support different from the magnetic field, whose resulting force serves the purpose of contrasting the weight of the object, along with any other possible acceleration source[3]. Levitation based trains exploit the established dynamic equilibrium to generate a contactless runaway for travelling capsules: in this scenario, friction is limited to air resistance only, allowing *maglev* trains to reach speeds up to 600km/h, while fully relying on electrical propulsion.
Nevertheless, despite the enthusiasm about this technology, maglev trains are scarcely employed worldwide, since they are not enough economically sustainable:

the reached speed limit does not, at the moment, make the journey much faster than a short distance flight between the same start and end points, but it is much more expensive. To this end, the idea has been further exploited in the theoretical development of the *Hyperloop* concept, whose first proposal as a white paper dates back to 2013[4]. In the following section a more detailed description of this framework and its operation principle are reported.

1.2 *Hyperloop* technonolgy

The target route for which the first conceptual prototype has been developed is the one between major urban area whose distance is at most 1500km. The fundamental improvement with respect to maglev technology consists in the use of low-pressure tubes, so that levitating capsules, propelled by an electric motor, undergo as minimum air drag as possible. Therefore, speeds up to 1200km/h can be achieved: this feature becomes crucial in the above mentioned medium-range routes, since it allows to travel over major urban areas in a significantly short time.

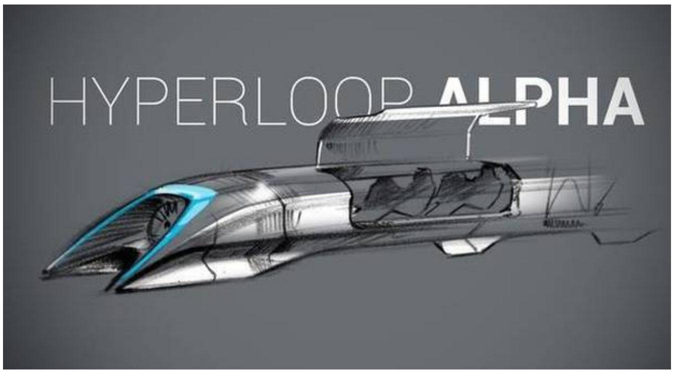

Figure 1.1: Hyperloop alpha, qualitative drawing [4].

1.2.1 Levitation system

In this technology, a key role is played by the levitation system. While the first draft introduced air bearings, the idea has recently evolved by replacing those with magnetic pads. Their operating principle is based on the Inductrack concept [5] and on electrodynamic levitation: moving capsules feature permanent magnets, which induce eddy currents on the conducting track as a result of Faraday-Lenz law. In turn, these currents close the magnetic circuit exerting two force components on the capsule:

- *lift* force F_L, on the vertical direction, it is responsible for levitation;
- *drag* force F_D, on the propulsion direction with opposite orientation, it acts as a friction terms, since it accounts for the reluctance of the circuit.

When compared to air bearings, permanent magnet based electrodynamic levitation is simpler and more self-reliable. Furthermore, this architecture does not require additional propulsion and provides a lift-to-drag ratio that is proportional to longitudinal velocity, thus being particularly interesting in ultra high speed applications. As a drawback, PM based levitation devices come with an intrinsically unstable behaviour.

1.2.2 Feasibility studies

Given the amazing capabilities of the above introduced technology, as well as the outcomes of its successful implementation, experimental validation and feasibility studies have been carried out in recent years. In particular, General Atomics[6] has developed, in ccoperation with the Federal Transit Administration (FTA), a 120m long maglev test track in California. Tests on system dynamics and journey quality have been performed. Despite the absence of a low-pressure environment, the levitation system under test resembles the one of the modern *Hyperloop*: permanent magnets arrays are attached to the cart, which is propelled by a linear induction motor. Levitation and guidance occur due to the interaction between the cart and an electrically conductive runaway.
The results of the experimental campaign are excellent in terms of lift-off velocity and lift-to-drag forces ratio. However, both levitation and guidance steady-state airgaps were larger than expected, but bounded by auxiliary wheels: such behaviour masks the above mentioned intrinsic instability of the levitation system.

Relevant results in stabilisation and experimental characterisation of the *Hyperloop* levitation have been achieved by students taking part in the SpaceX Hyperloop Pod Competition[7]. However, these efforts are entirely based on numerical simulations, and no analytical approach was followed to rigorously capture such important property of the system.

1.3 Literature review

This section deals with a synthetic literature review, through which the experimental work described in the forthcoming chapters is contextualised among state-of-the-art research.
In the past years, the unique and cross-branches concepts that make up the Hyperloop technology have been subject to investigation by the scientific community.

Recent research efforts tackle several aspect of the system, such as its framework [9], aerodynamic behaviour [10] and thrust [11, 12]. Electrodynamic levitation is instead the nucleus of up-to-date works[13], being it a relatively uninvestigated field. In particular, research has been made on technique to implement stable and passive levitation devices, as previously mentioned: the framework of electrodynamic bearings for rotating machines sets the pillars to develop its translational counterpart. EDBs have been, in fact, subject of substantial research efforts by Tonoli et al.[14, 15], Filatov and Maslen [16], Lembke[17, 18], in terms of modelling, instability identification and development of stabilisation techniques.
Translational EDBs share with their rotational equivalent the unstable behaviour, which was successfully modelled by Post and Ryutov[5], but not observed in successive experiments[19].
Several up-to-date works have tackled modelling and identification of linear levitation devices, but they do not address its mechanical behaviour, where, instead, instability takes place: in particular, stabilisation and experimental assessments of the above described levitation device have been carried out by university students teams taking part in the Space X Hyperloop Pod Competition [20, 7], as well as by several research groups, whose work was unable to rigorously assess instability of the system [7, 21].
A recent research effort by Guo et al.[22] proposes an electrical circuit based model for deriving static levitation forces from the governing electrodynamic laws; this approach is used in its nonlinear version, based on the magnetic vector potential approach, to optimise the geometry of the system[24, 23]. Nevertheless, neither of these studies deal with the mechanical dynamical behaviour of the system, thus failing in capturing instability phenomena. This feature has been demonstrated through an heuristic method by Wang et al.[25, 26], whose two degrees-of-freedom model for Inductrack based systems accurately describes levitation only from an electrodynamic viewpoint. Moreover, possible stabilisation techniques were not dealt with by the authors.

1.3.1 Multi-body approach to modelling of linear electrodynamic levitation devices

In this context, the works proposed by Galluzzi et al. and Circosta et al. [8, 27] establish a multidomain linear modelling technique that succeeds in accurately describing the electrodynamic levitation phenomenon when coupled with mechanical domain variables.

Such approach is based on discretisation of the otherwise distributed parameter model for the conductive track by means of a multiple branch RL circuit. Numerical data coming from finite element simulations are fitted to the novel linear time invariant description of the system, until a number of branches N_b that optimises

fitting quality and modelling complexity is found.
Through this simpler mathematical description, in the framework of linear time-invariant systems, the intrinsic unstable behaviour is successfully identified for each degree-of-freedom, and the definition of a suitable stabilisation technique is straightforward.

1.4 Thesis goal

These premises highlight the absence of a rigorous experimental validation of accurate models of translational EDBs; such a work plays, instead, a crucial role in fostering the development of the *Hyperloop* technology. To this end, the thesis proposes a design procedure for a test rig to assess the identification and dynamic behaviour of a *Hyperloop*-like levitation device, in a laboratory scale. In particular, its main focus is the validation of a multi-domain modelling technique proposed by Galluzzi et al.[8], that allows analytical stabilisation of the system through additional damping. The second fundamental point is the physical implementation of the above defined stabilisation technique, addressed through suspension design and control.

1.4.1 Outline

The remainder of this work is organised as follows. The subsequent two chapters deal with preliminary assessments and modelling activities: at first an insight is provided on the structure of the test rig by comparing and contrasting different bench architectures motivating the final choice. Afterwards, relevant features of the measurement systems are discussed.
Therefore, after having introduced the fundamental theoretical concepts, linear parameters that describe the system under test are identified on the basis of the above defined multi-domain approach, and stability analysis of the whole levitation device is performed.
A further chapter tackles the problem of bearings selection and the calculation of their frictional moment.

Afterwards, suspension design and control are illustrated: starting from the stability analysis carried out in the previous chapter, the choice of a voice coil actuator as a damping device is discussed, along with the fundamental characteristics of the selected item. Several control architectures are compared in terms of performances and complexity.

The sixth chapter deals with validation of the previously discussed suspension control algorithms, and providing final considerations on the project and possible future improvements. In particular, a feasible input longitudinal speed profile is discussed, and results of numerical simulations for the proposed control strategies are reported and discussed. Then, a possible solution that gathers the controller with the necessary interfaces, to be deployed on the target MCU is proposed: the outcomes of a preliminary functional tests are discussed.

At last, conclusion on the peformed activities are drawn, and proposals for further insights and future studies are provided.

Chapter 2

Test bench layout

This chapter discusses the main steps that were tackled during the preliminary design of the experiment. In particular, assumptions, measured physical variables and expected outcomes are introduced in the first section, along with the layout of the main experimental frame. The forthcoming sections address the description of the measurement systems and at last, of the permanent magnet Halbach arrays to be used for electrodynamic levitation.

2.1 Main frame description

The purpose of the experiment consists in validating analytical and numerical results of the studies discussed in Chapter 1.3, in terms of linear model parameters verification -through lift and drag force evaluation-, and optimal stability conditions assessment -through dynamic behaviour investigation. Therefore, two different test setups are required. In particular, lift and drag forces are measured in quasi-static conditions, i.e. constant longitudinal velocity v and airgap z_p: therefore, it is sufficient to connect the PM array to a mass m_t that represents the whole capsule. On the other hand, the introduction of the secondary suspension as described in Section 3.2.3, is necessary to analyse the stability (i.e. dynamic behaviour) of the levitation device. Furthermore, the system must be able to perform vertical displacement.

In both cases, relative longitudinal velocity between the capsule and the track must be guaranteed. The straightforward solution of a linear runaway is not feasible in terms of overall bench dimensions, since it should be long enough to run experiments for the time needed to measure variables of interest. Nevertheless, bench footprint dramatically decreases if a circular crown shaped track with diameter D is built on a disk with diameter D', that is kept running by an electric motor. Defining L_t as the total length of the PM array in the longitudinal direction, a sufficiently large D/L_t ratio (i.e. $D/L_t \geq 10$) allows to approximate the direction of the tangential velocity vector $\mathbf{v}$ as constant over the pad length.

2.1.1 Relative orientation selection

In this framework, two arrangements are possible in terms of orientation of the runaway, disk and motor, by exploiting either axial or radial symmetry. A qualitative schematic representation of those is provided in Figure 2.1 and Figure 2.2 respectively.

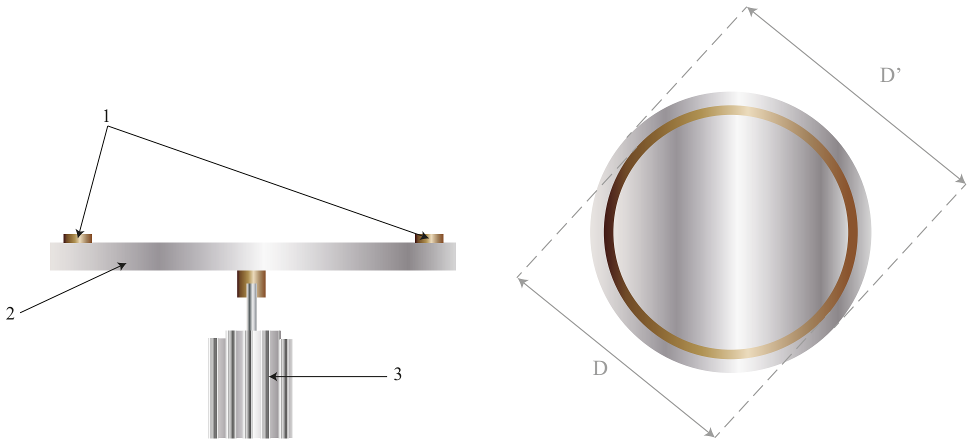

(a) Front view **(b)** Top view

Figure 2.1: Frame layout: axial symmetry. 1. Track; 2. Rotating disk; 3. Motor

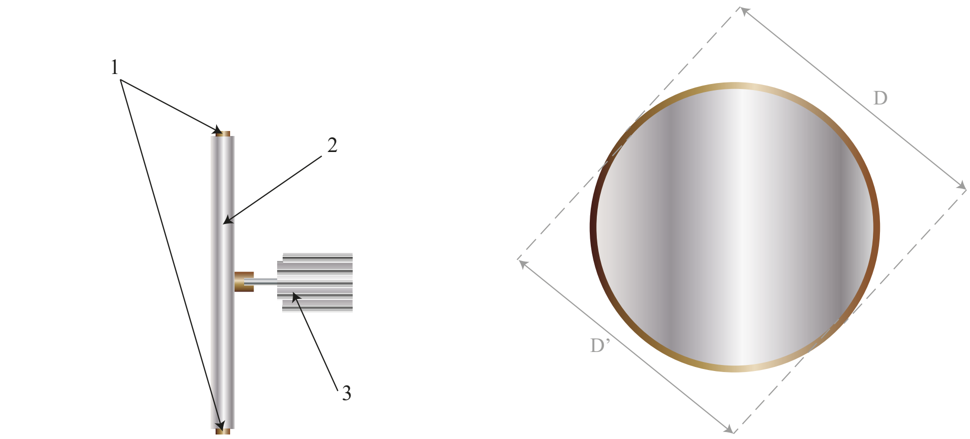

(a) Side view **(b)** Front view

Figure 2.2: Frame layout: axial symmetry. 1. Track; 2. Rotating disk; 3. Motor

The most relevant structural difference between the two frames consists in the position of the runaway, that lies on the base surface of the disk in the axial layout and on its lateral surface for the radial symmetry based solution. Nevertheless, in both cases constant airgap through the whole length of the capsule is not guaranteed *a priori*, due to different phenomena.
In the axial structure the issue is caused by mechanical vibrations. In particular, the one-diameter mode of the disk yields conical motion, that can originate large airgap variations. However, this problem can be tackled through mechanical design in order to minimise the amplitude of such mode.
Track curvature is instead crucial for the radial symmetry based solution: hence the necessity of either choosing a higher D/L_t ratio with respect to the axial frame, that impacts on the overall dimensions of the frame, or employing curved magnets to build the Halbach array. On the contrary, the dynamic behaviour of the disk has minimal influence on the performances of the measurement system.

In light of this comparison, the chosen solution is the axial symmetry based frame: it can feature a smaller footprint, since a lower D/L_t ratio can be employed, it does not require magnets that follow the curvature of the runaway -which would result in higher costs-, and its main issue can be dealt with during the design phase. Figure 2.3 shows a section view of the refined assembly of the frame. A steel structure surrounds the disk and the track on top of it, and it acts as a fixed supporting structure for the measurement systems, to be described in the forthcoming sections, while guaranteeing safety during experiment monitoring. The disk is connected to the electric motor to be used for propulsion through a torsional joint and a shaft. The latter is supported by single row angular contact ball bearings, whose selection procedure is discussed in Chapter 4.

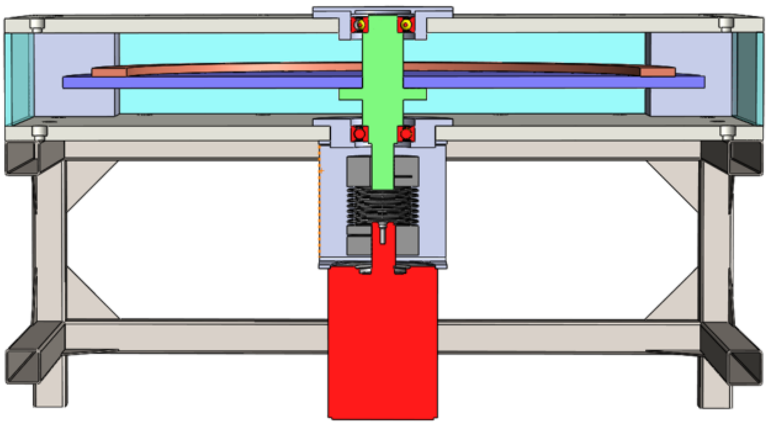

Figure 2.3: Test bench main frame: section view. Courtesy of Dr. A. Bonfitto, Eng. E.C. Zenerino and A. D'Oronzo.

2.2 Measurement system: quasi-static test

A possible arrangement that is suitable for static force evaluation is reported in the 3D drawing in Figure 2.4, where the call-out balloons (henceforth C.B.) point out the fundamental items within the assembly.

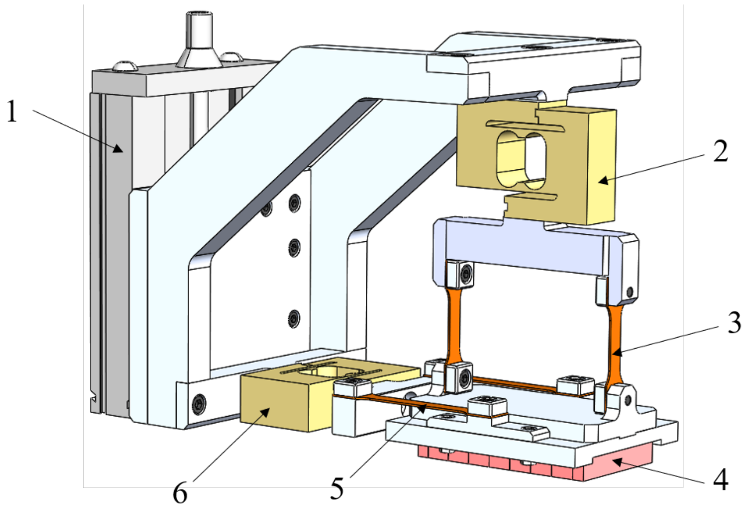

Figure 2.4: Measurement system for quasi-static test. Courtesy of Dr. A. Bonfitto, Eng. E.C. Zenerino and A. D'Oronzo.

The *micrometric linear stage* (C.B. 1) is employed to impose the distance between the runaway and the PM array, that is the constant airgap z_p. Lift and drag forces are measured through *load cells* (C.B. 2 and 6 respectively), that are connected to the *magnets arrangement* (C.B. 4) by means of *flexure hinges*, that serve the purpose of decoupling the degrees of freedom within the measurement process.

2.3 Measurement system: dynamic test

The test setup to evaluate the dynamic behaviour of the levitation system is reported in the 3D assembly in Figure 2.5 with different views. In addition, Figure 2.6 shows a two-dimensional layout which helps visualising all the elements that are featured in the 3D representation in an intuitive manner.
Here too, the micrometric linear stage (C.B. 1) is required to impose the initial airgap z_{p0} between the track and the Halbach array (C.B. 2). Sprung and unsprung masses (C.B. 3 and 7 respectively) are linked by means of the secondary suspension,

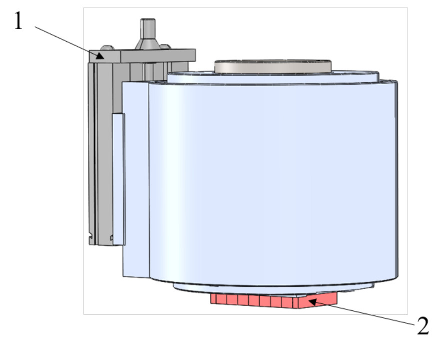

(a) Isometric view

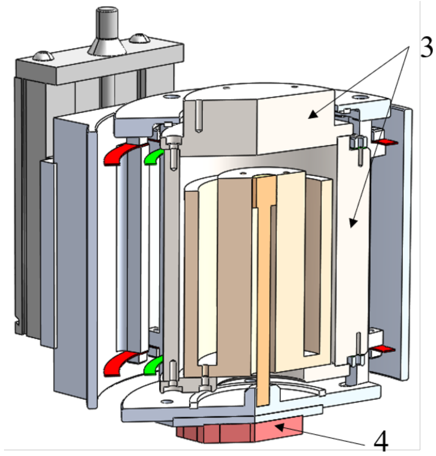

(b) Section view

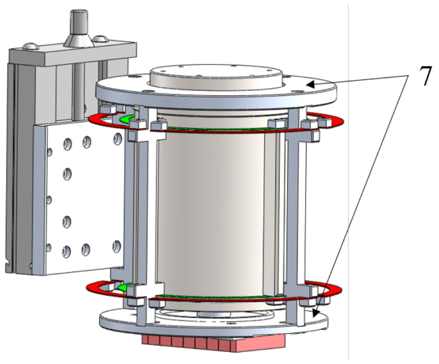

(c) Isometric view 2

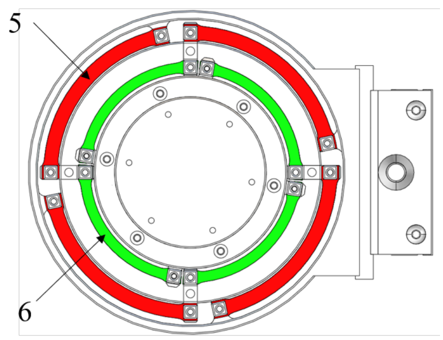

(d) Bottom view

Figure 2.5: Measurement setup for dynamic test. Courtesy of Dr. A. Bonfitto, Eng. E.C. Zenerino and A. D'Oronzo.

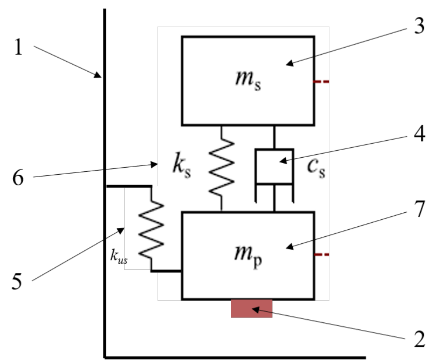

Figure 2.6: Dynamic test layout, 2D scheme

that is composed of a voice coil[1] (C.B. 4) that can be tuned to introduce damping in the system, and of sprung-unsprung mass springs (C.B. 6), that account for the stiffness k_s (see Section 3.2.3). In particular, they are arranged as two layers of curved leaf springs: such layout is needed to prevent relative rotation and longitudinal displacement between the capsule and the bogie.
The same technique is employed to connect the unsprung mass to the micrometric stage, that acts as a stator, by means of springs with stiffness k_{us} (C.B. 5).

2.4 Halbach array configurations

To better assess the quality of the linear model proposed in *Galluzzi et al.*[8], validation will be performed on different magnets arrays. Their principal dimensions (see Figure 3.2 for the reference frame), magnets' polarisation orientation[2] and number of pole pairs are reported in Table 2.1.
In order to impose $D/L_t \approx 10$, magnets configurations shall undergo re-dimension by acting either on the scale or on the number of pole pairs: such choices are summarised in the last two columns of Table 2.1, and motivated on the basis of design specifications discussed in Chapter 3. One can notice that the proposed scale factor makes *Post/HTT single bogie* and *Publication pod* equivalent.

	Initial configuration			Test bench arrangement	
ID	Size (x, y, z)	Magnet orientation	Pole pairs	Scale	Pole pairs
Post/HTT single bogie	$(2, 10, 2)$[in]	90°	4	1:4	2
Publication pod	$(1, 5, 1)$[in]	90°	2	1:2	2
Post/Alex single bogie	$(2, 10, 2)$[in]	45°	2	1:4	1
Post/Arash Best payload to drag	$(4, 6, 3.5)$[in]	90°	1	1:8	2

Table 2.1: PM arrangements subject to validation

[1]Motivations on the use of a voice coil actuator as damper are found in Chapter 5.

[2]It is expressed in degrees as the angular difference on the polarisation direction between adjacent magnets.

Chapter 3

Modelling and identification

This chapter describes the modelling activities that have been carried out to identify a suitable multi-domain description of the levitation device in the LTI systems framework. After having summarised the main steps, design specifications are introduced and commented. Afterwards, assumptions and results of analytical and numerical approaches are discussed.

3.1 Activity goals and design specifications

The proposed modelling approach consists of several different steps, as graphically described in Figure 3.1.

1. At first, the electrodynamic levitation phenomenon is modelled and simulated by means of finite element modelling methodologies, to retrieve lift and drag forces in quasi-static conditions.

2. Upon their values a system identification procedure is carried out, to characterise a linear lumped parameters representation that suitably reproduces the nonlinear electromagnetic interaction between the permanent magnets array and the conductive track. The target model is a multi-branch R-L circuit (as in Ref.[8]), where the total number of branches N_b is a design parameter that can be tuned to obtain a trade-off between model complexity and fit quality.

3. Afterwards, the resulting bogie model is coupled with the mechanical domain formulation of the capsule (which can be represented as a quarter-car model), to obtain a single LTI system that completely describes the experiment.

4. In this framework, the unstable behaviour of the system can be rigorously assessed and removed, by introducing variable additional damping through a secondary suspension. Stability can be optimised through root locus analysis.

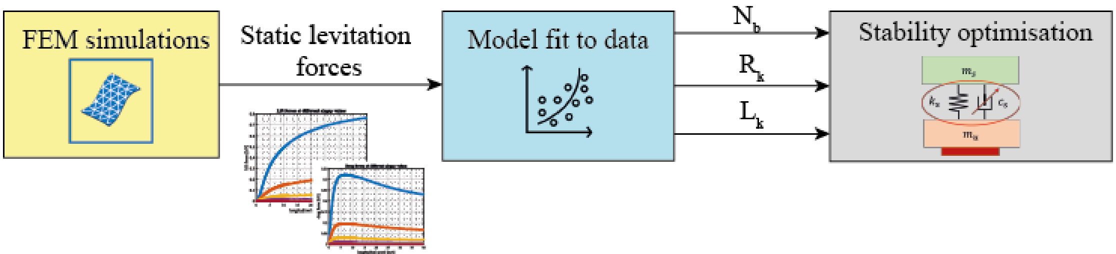

Figure 3.1: Modelling activities: flowchart

The forthcoming sections provide detailed description of the above mentioned procedures, along with relevant results. Prior to this, requirements on significant physical variables are discussed and motivated.

3.1.1 Design specifications

The most relevant limitations to the static forces values, and in particular on the drag force, comes from the electric motor's maximum absolute ratings in terms of power and torque. In particular, the AKM74L Kollmorgen®(datasheet on Ref. [28]) shall be used for propulsion; as a consequence, power and torque to win the drag force as a function of the longitudinal velocity v and of the airgap z_p, shall not exceed the above mentioned limiting values.
A further parameter to be investigated is the position of the electrical pole, that corresponds to the peripheral velocity value v_p where F_D is maximum: in order to properly observe the force-velocity relation, speeds up to $5v_p$ shall be observed. However, given the structure of the bench, the maximum feasible peripheral speed is around $v_{max} = 40\text{m/s}$: therefore, the drag force peak shall occur, at most, at $v_p \approx v_{max}/5 = 8\text{m/s}$.
These requirements are summarised in Table 3.1.

Description	**Expression**	**Value**	**Unit**
Disk diameter	D	1	m
Maximum peripheral velocity	v_{max}	40	m/s
Position of the electrical pole	v_p	8	m/s
Minimum airgap	z_{pmin}	1	mm
Electric motor maximum power	P_{max}	5.47	kW
Electric motor rated torque	T_{max}	49.7	Nm
Electric motor rated speed	Ω_{max}	1200	rpm

Table 3.1: Design specifications summary

3.2 Theoretical background

3.2.1 Problem formulation

The solution for a linear electrodynamic levitation system proposed by Post & Ryutov features the interaction between a Halbach array of permanent magnets in a NdFeB alloy attached to the cart, and an electrically conductive aluminium track (Figure 3.2). Relevant geometric and physical parameters may be read in Table 3.2.

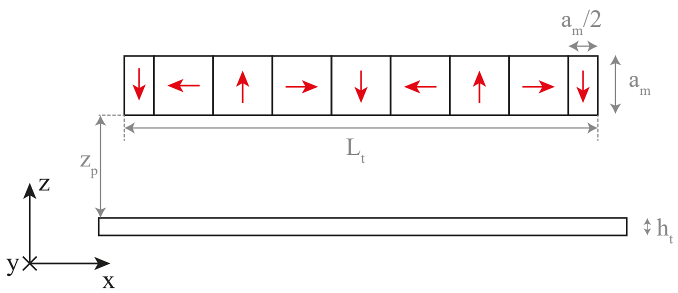

Figure 3.2: Halbach array

Item	Description	Symbol	Value	Unit
N45UH NdFeB PM array	Number of pole pairs	N_p	2	-
	Number of magnets per pole pair	N_m	4	-
	Magnet side length	a_m	25	mm
	Magnet in-plane depth	d_m	125	mm
	Remanent magnetic flux density	B_r	1.29	T
	Resistivity	ρ_m	181.44	$\mu\Omega$cm
	Relative magnetic permeability	$\mu_{r,m}$	1.06	-
6101-T61 aluminium track	Thickness	h_t	12.7	mm
	Resistivity	ρ_t	3.51	$\mu\Omega$cm
	Relative magnetic permeability	$\mu_{r,t}$	1	-

Table 3.2: Levitation system: geometric and physical parameters

Such peculiar arrangement of the magnets' polarisation direction allows to produce a periodic field on the surface that faces the runaway, and null out-of-plane components on the opposite side.
Both the PM array and the aluminium slab are subject to electromagnetic phenomena that can be described through Equations 3.1-3.3, that account for, respectively, the relation between the magnetic field **H** and the current density **J** within each

medium (third Maxwell's equation), the Lorenz force contribution on the track current density, due to the longitudinal velocity v, and the link between the magnetic field and the magnetic flux density $\mathbf{B}$ (Ampére's law).

$$\nabla \times \mathbf{H} = \mathbf{J} \tag{3.1}$$
$$\mathbf{J} = \sigma \left(\mathbf{v} \times \mathbf{B}\right) \tag{3.2}$$
$$\mathbf{B} = \mu_0 \mu_r \mathbf{H} \tag{3.3}$$

3.2.2 Equivalent lumped parameters model

Although the equations point out the existence of strongly nonlinear phenomena, *Galluzzi et al.* propose a linearisation method that allows to represent the levitation device through a lumped parameters approximation: the model consist in a parallel of N_b branches (Figure 3.3), each with its own resistance R_k and inductance L_k, driven by a voltage E.

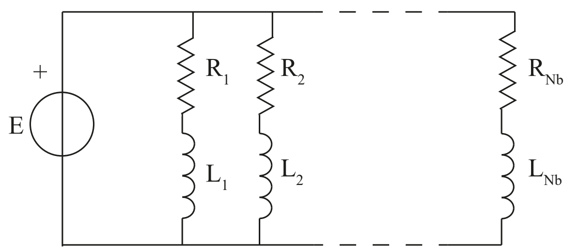

Figure 3.3: Lumped parameter model that describes the interaction between the PM array and the track.

In this framework, the branches provide discretisation of the otherwise continuous current density distribution over the track. The voltage source E, instead, accounts for back electromotive force phenomena, due to the time varying flux linkage λ generated by the PM array. The governing equations of this circuit are easily written in the phasor domain, using a reference frame that is fixed to the aluminium runaway. Furthermore, the model successfully describes the interaction with physical quantities in the mechanical domain through its power balance: lift and drag forces are easily retrieved from the mechanical energy.

Assuming constant airgap z_p and longitudinal velocity v (see Figure 3.2), levitation and drag are computed on the nonlinear system through static, two-dimensional FEM simulations at different velocities (from 0m/s to 340m/s) and airgap values. Planar geometry description is possible due to the relation $d_m > N_m a_m/2$: this reasonably large value for the in-plane depth allows to ignore boundary effects on the eddy current distribution. These data allow to perform a least-square fitting on static forces expression derived with the proposed linear model, in terms of

equivalent resistance and inductance, in order to optimise N_b. This method has proven that a number of branches that appropriately reproduces the forces-velocity relations is $N_b = 3$.
Levitation forces assume the expression in Equations 3.4 and 3.5, while the description of the featured parameters can be read in Table 3.3.

$$\bar{F}_L = \frac{\Lambda_0^2}{\gamma} = e^{-2z_p/\gamma} \sum_{k=1}^{N_b} \frac{\omega^2/\omega_{p,k}^2}{L_k\left(1+\omega^2/\omega_{p,k}^2\right)} \tag{3.4}$$

$$\bar{F}_D = \frac{\Lambda_0^2}{\gamma} = e^{-2z_p/\gamma} \sum_{k=1}^{N_b} \frac{\omega/\omega_{p,k}}{L_k\left(1+\omega^2/\omega_{p,k}^2\right)} \tag{3.5}$$

Description	Expression	Measurement unit
Number of magnets per pole pair	N_m	-
Pole pitch ratio	$\gamma = N_m a_m/2\pi$	-
Complex rotational velocity	$\omega = v/\gamma$	rad/s
Flux linkage	Λ_0	Wb

Table 3.3: Levitation forces parameters

Branch resistance R_k and inductance L_k define its natural frequency $\omega_{p,k}$ as in Equation 3.6.

$$\omega_{p,k} = \frac{R_k}{L_k} \tag{3.6}$$

3.2.3 Stability analysis

The derivation of a suitable linear model allows to formulate the problem in state-space representation. As a consequence, its stability properties are assessed by evaluating the eigenvalues of the state matrix for increasing longitudinal velocities v. This analysis has pointed out that a one degree of freedom arrangement, composed of a mass m_t rigidly attached to the PM array is not able to provide internal stability for velocities higher than 6.4m/s.

Nevertheless, stable operation throughout the whole speed range can be achieved through additional damping. This feature can be introduced by means of a suspension between the capsule and the magnets array: therefore, the levitation system is a two degrees of freedom Quarter Car Model (Figure 3.4).

The total mass is decoupled in $m_t = m_s + m_p$, where m_s accounts for the mass of the cart (sprung mass), while m_p is the mass of the pad and of the required connections (unsprung mass). The suspension can be modelled as a parallel connection of a linear spring with stiffness k_s and of a viscous damper c_s.

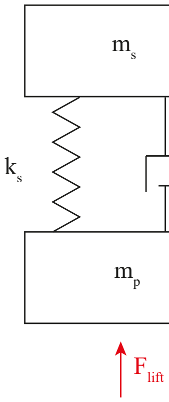

Figure 3.4: Two degrees of freedom levitation system: quarter car model

Here, k_s is regulated to obtain a sprung mass natural frequency equal to 1Hz, in order to ensure passenger comfort and hinder motion sickness, according to the ISO 2631-1 standard[29]. The damping c_s is instead tuned to achieve the optimal stability condition, which can be identified as the maximum horizontal gap between each pole and the imaginary axis. In particular, the most unstable pole p_i is identified as the one with highest real part, and its evolution as a function of c_s is subject to minimisation, yielding to the optimal damping value c_{opt}, and corresponding global minimum $\Re(p_i(c_{opt}))$.

3.2.4 Generalisation to multiple degrees-of-freedom

Frequency and time domain numerical validation has assessed the validity of the proposed model with respect to the nonlinear version both in vertical dynamics and in multi-degrees of freedom scenarios, which feature a more realistic, three-dimensional representation of the levitation system, as discussed by Circorsta et al. In particular, said degrees of freedom are modelled by replicating the approach that has been followed to characterise the vertical dynamics, having uncoupled the DOFs. Therefore, the additional suspension is designed in terms of damping by optimising the stability property of the levitation system. Such approach has been tested on a multibody model with fewer approximations, to investigate the behaviour of the system in terms of coupling and rejection of track flaws.

3.3 FEM simulations and lumped parameter model identification

Given the requirements in Table 3.1, and the above outlined procedure, the first activity consists in developing a mathematical model that describes the interaction between the permanent magnets array and the copper track. To this end, the FE COMSOL Multiphysics®has been employed, and the procedure has been carried out for the PM arrays described in Section 2.4. The simulation framework is represented in Figure 3.5, and it is composed of three domains.

1. **N45UH permanent magnet Halbach array**

2. **6101-T61 aluminium track**

3. **Air surroundings**

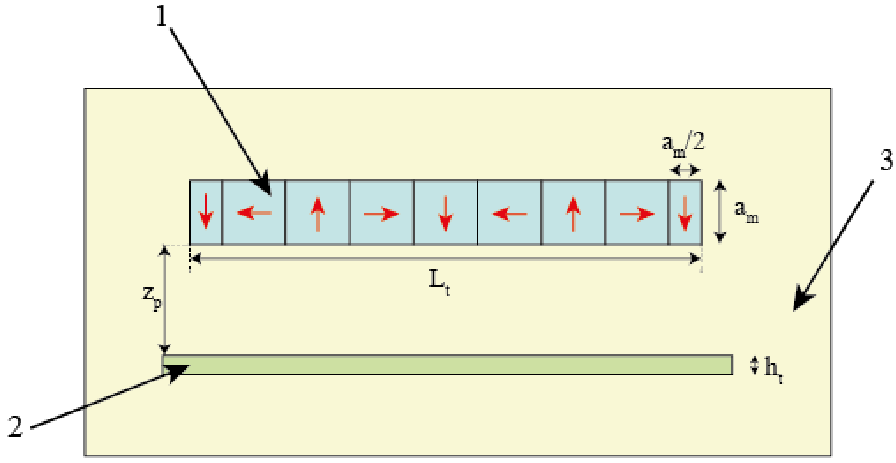

Figure 3.5: FE simulation layout

These were meshed by means of a triangular distribution that counts up to 18 thousands elements approximately. In particular, in order to guarantee a sufficiently accurate eddy current replication, the maximum mesh size for the copper runaway domain has been adjusted to 2mm. Prior to performing quantitative analysis on quasi-static forces, a suitable runaway thickness value h_t must be selected in order to minimise the eddy current density at the bottom surface of the track. In practice, the model has been solved for the magnetic vector potential $\mathbf{A}$ (subject to the relation in Equation 3.7), Equations 3.1-3.2.

$$\mathbf{B} = \nabla \times \mathbf{A} \tag{3.7}$$

Track width optimisation has been performed on a sufficiently low airgap value $z_p = 1$mm, since the entity of the electrodynamic interaction is much stronger for small gaps. Furthermore, eddy current penetration is a more relevant phenomenon at low speed, since the skin effect becomes predominant with higher velocities, and the increasing lift force yields an increment in z_p (as levitation counteracts weight), thus reducing the overall current density. As a consequence, the investigation has been carried out through a trial and error variation of h_t, and satisfactory results (Figure 3.6) are achieved for all the magnets arrangements when $h_t = 0.55\text{in} \approx 14\text{mm}$.

3.3.1 Linear system identification: aluminium runaway

On the basis of the above derived track width value, lift and drag forces, positive along z and $-x$ respectively, have been retrieved in stationary conditions: the model is simulated for all constant horizontal velocities v within the range $[0 \div 80]$m/s, and for all airgap values in the range $[5 \div 35]$mm.

Afterwards, these data have been used to identify the lumped parameters RL model with a variable number of branches N_b. In particular, the above mentioned FE output signals have been fitted to Equations 3.8-3.9, by minimising the ℓ_2 norm of the fit errors $\Delta_L = \bar{F}_L - F_L$ and $\Delta_D = \bar{F}_D - F_D$. Their values for the three examined configurations have been reported in Table 3.4.

$$\bar{F}_L = \frac{\Lambda_0^2}{\gamma} = e^{-2z_p/\gamma} \sum_{k=1}^{N_b} \frac{\omega^2/\omega_{p,k}^2}{L_k\left(1+\omega^2/\omega_{p,k}^2\right)} \tag{3.8}$$

$$\bar{F}_D = \frac{\Lambda_0^2}{\gamma} = e^{-2z_p/\gamma} \sum_{k=1}^{N_b} \frac{\omega/\omega_{p,k}}{L_k\left(1+\omega^2/\omega_{p,k}^2\right)} \tag{3.9}$$

	$N_b = 1$	$N_b = 2$	$N_b = 3$	$N_b = 4$
				N
Post/HTT	588.25	139.04	121.66	121.41
Post/Alex	628.44	177.96	171.02	170.96
Post/Arash	156.97	34.89	29.87	29.8

Table 3.4: Force fit error over linear model's number of branches N_b

These data suggest that the eddy current distribution may be well approximated by means of a $N_b = 3$ RL parallel branches, given the negligible difference in terms of fit error between $N_b = 3$ and $N_b = 4$; as a consequence, one can assess the validity of the proposed approach even if a scale factor is applied. Figures 3.11-3.13 show a comparison between simulation data (markers) and forces computed in the linear framework (solid lines), with airgap ranging from $z_p = 5$mm (blue) to $z_p = 35$mm (purple). However, just one of the three arrangements (Post/Alex single bogie) is compliant with the specifications on the maximum $v_{p,k}$, as highlighted in Table 3.5.

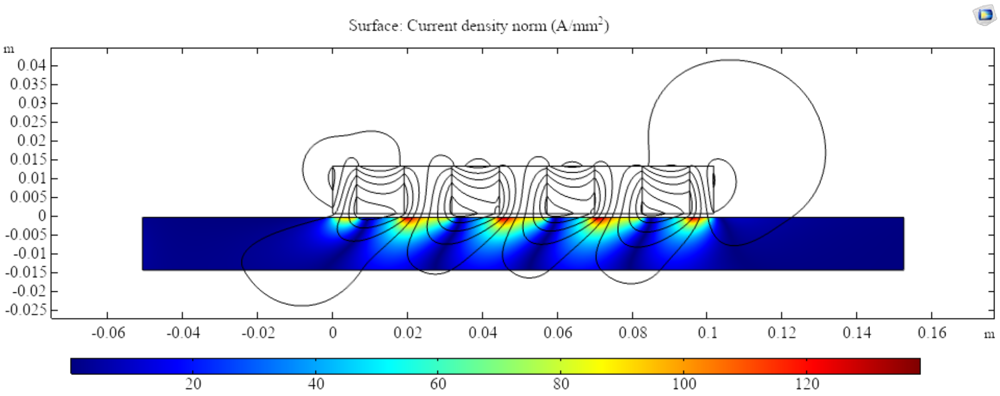

(a) Post/HTT single bogie

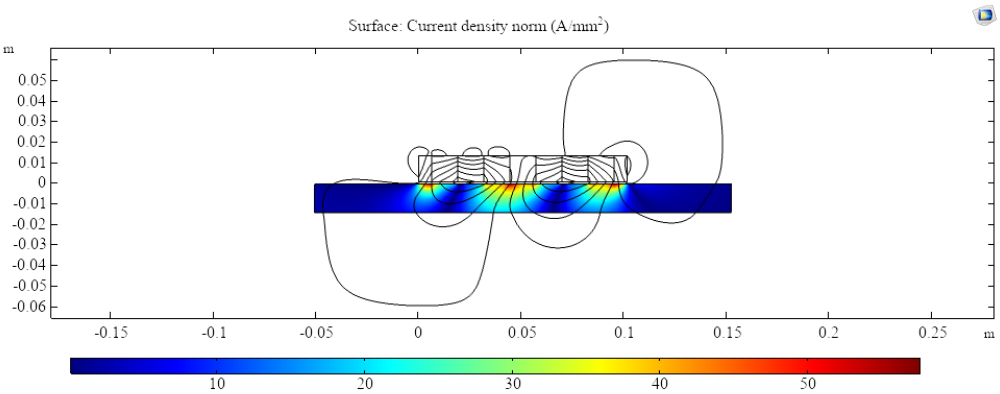

(b) Post/Alex single bogie

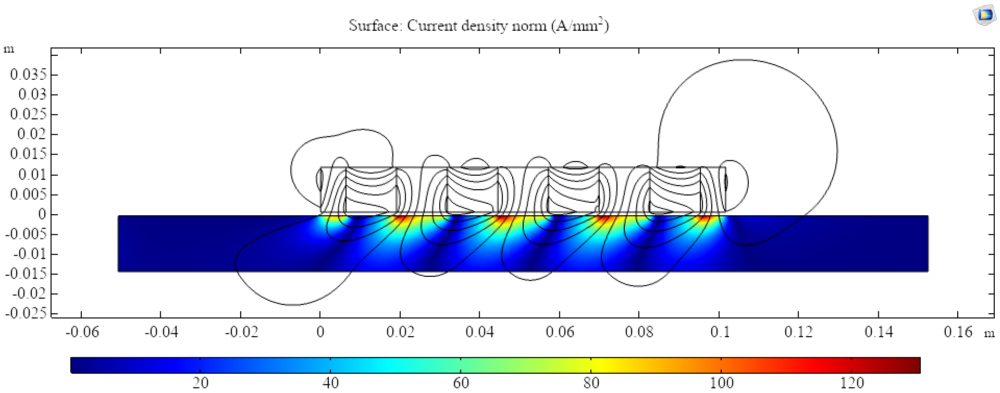

(c) Post/Arash best payload to drag

Figure 3.6: Eddy currents distribution within the track, $h_t = 14$mm

To address this issue, one can further act on the scale factor and, in order to keep $D/L_t \approx 10$, on the diameter of the circular track. Therefore, a possible solution

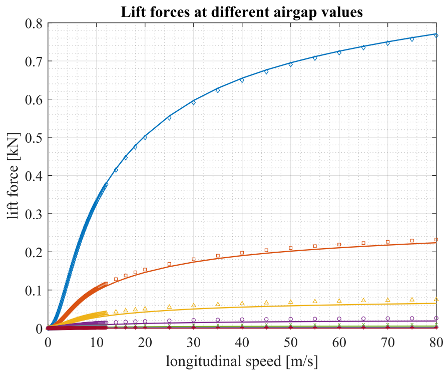

(a) Lift forces

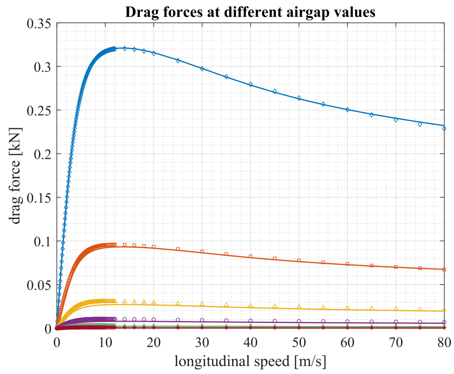

(b) Drag forces

Figure 3.7: Post/HTT single bogie

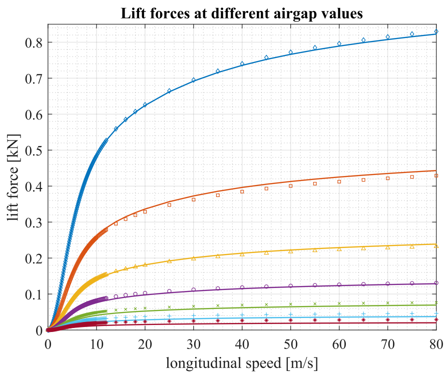

(a) Lift forces

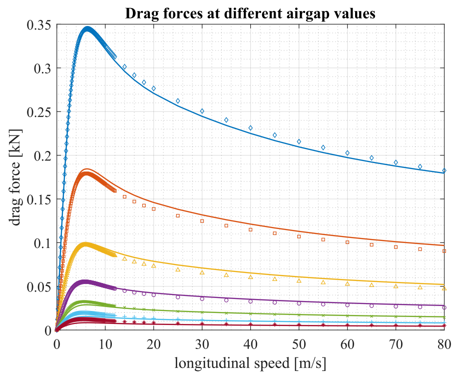

(b) Drag forces

Figure 3.8: Post/Alex single bogie

	Post/HTT	Post/Alex	Post/Arash
$v_{p,k}$, m/s	12	5.8	11.8

Table 3.5: Electrical pole position

consists in increasing D to 1.5m, and applying the scale factors in Table 3.6 to the PM arrays under test.

Despite this strategy yields results that are compatible with the specifications on $v_{p,k}$, the overall bench footprint is not compliant with the maximum allowable dimensions of the site where the experiment shall be carried out. Moreover, the increase in disk diameter by 0.5m yields a much more unpredictable behaviour in terms of rotordynamics, thus complicating the mechanical design by a far too large amount.

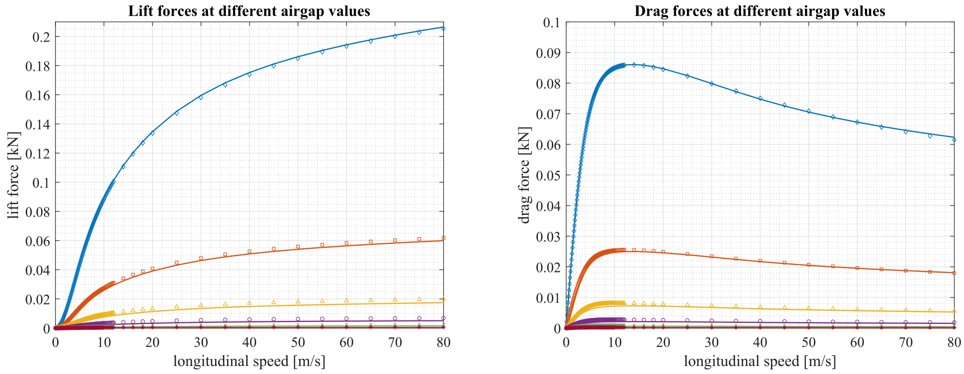

(a) Lift forces **(b)** Drag forces

Figure 3.9: Post/Arash best payload to drag

	Initial configuration		Test bench arrangement		Electrical pole position
ID	Size (x, y, z)	Pole pairs	Scale	Pole pairs	$[m/s]$
Post/HTT single bogie	$(2, 10, 2)$[in]	4	1:3	2	5
Publication pod	$(1, 5, 1)$[in]	2	2:3	2	5
Post/Alex single bogie	$(2, 10, 2)$[in]	2	1:3	1	3
Post/Arash Best payload to drag	$(4, 6, 3.5)$[in]	1	1:6	2	4.9

Table 3.6: PM arrangements subject to validation, $D = 1.5$m

3.3.2 Linear system identification: copper track

The above discussed analytical studies assume the use of an aluminium track, in compliance with Hyperloop Pod competition specifications[30].
Nevertheless, the quality of the experiment can indeed be improved if a material with better conduction characteristics is employed. In particular, a suitable solution features a *Oxygen Free Electronic* copper runaway; its resistivity at $60°C$ is $1.72\mu\Omega cm$ [31, 32], which is significantly lower than the one for the aluminium alloy reported in Table 3.2. This property should yield smaller values for the equivalent lumped resistances R_k, and in turn, lower electrical pole frequencies $\omega_{p,k}$. As a consequence, both the evolution of lift and drag forces in quasi static conditions and the steady-state behaviour during the dynamic test could be fully described

within a smaller longitudinal velocity range, as prescribed by the specifications in Table 3.1.
Even in this case, a track width equal to $h_t \approx 14$mm yields an acceptable eddy currents distribution, as highlighted in Figures 3.10a-3.10c.

Following the same procedure that has been described for the aluminium track framework, quasi-static lift and drag forces derived through FE simulations are used as input for the linear system identification procedure. The fit error as a function of the number N_b of RL branches in Table 3.7 implies the conclusion that the proposed approach can well-represent the behaviour of the eddy currents within the track even when a material with different characteristics is used. Also in this case, $N_b = 3$ represents a good trade-off between fit accuracy and model complexity.

	$N_b = 1$	$N_b = 2$	$N_b = 3$	$N_b = 4$
				N
Post/HTT	199.68	50.01	35.17	34.92
Post/Alex	821.17	228.65	203.22	202.99
Post/Arash	200.37	49.9	35.23	34.99

Table 3.7: Force fit error over linear model's number of branches N_b

Nonlinear and linear system's static forces as a function of horizontal velocity and airgap values can be found in Figures 3.11-3.13. As it can be further inspected in Table 3.8, where identified parameters can be read, all the configurations exhibit compliant characteristics with the limitation on the maximum allowable electrical pole position.

	L_k [H]	R_k [Ω]	$\omega_{p,k}$ [rad/s]	$v_{p,k}$ [m/s]
Post/HTT single bogie	$7.13 \cdot 10^{-9}$	$5.88 \cdot 10^{-6}$	824.63	7.9
	$7.41 \cdot 10^{-9}$	$24.48 \cdot 10^{-6}$	$3.3 \cdot 10^{3}$	
	$11.35 \cdot 10^{-9}$	$228.39 \cdot 10^{-6}$	$20.13 \cdot 10^{3}$	
Post/Alex single bogie	$2.92 \cdot 10^{-15}$	$0.5 \cdot 10^{-12}$	170.86	3.5
	$5.87 \cdot 10^{-15}$	$5.55 \cdot 10^{-12}$	994.85	
	$9.19 \cdot 10^{-9}$	$51.32 \cdot 10^{-12}$	$5.58 \cdot 10^{3}$	
Post/Arash Best payload to drag	$0.4 \cdot 10^{-9}$	$0.16 \cdot 10^{-6}$	410.91	8
	$0.41 \cdot 10^{-9}$	$0.67 \cdot 10^{-6}$	$1.64 \cdot 10^{3}$	
	$0.62 \cdot 10^{-9}$	$6.16 \cdot 10^{-6}$	$9.91 \cdot 10^{3}$	

Table 3.8: Linear model parameters: summary

As far as power and torque specifications are concerned, it is necessary that they are satisfied over the whole velocity range for a given value of airgap z_p.

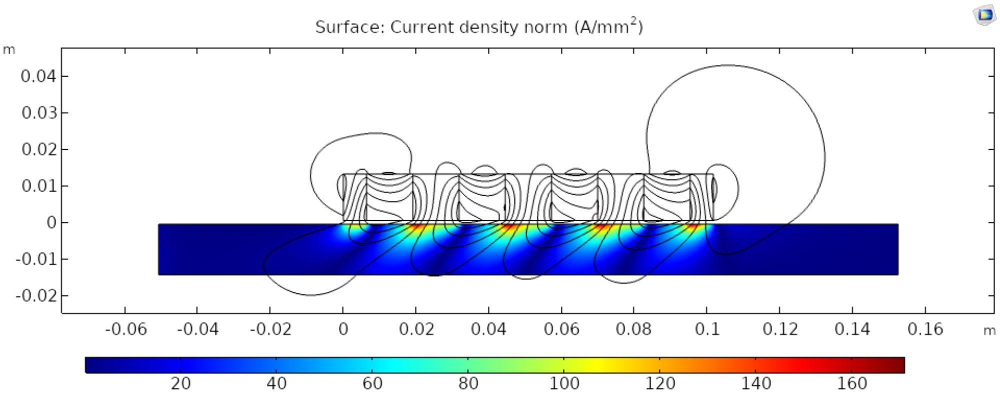

(a) Post/HTT single bogie

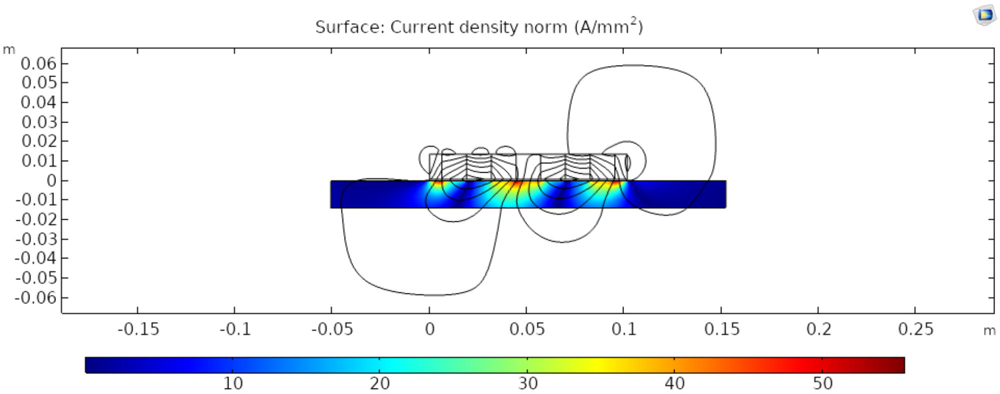

(b) Post/Alex single bogie

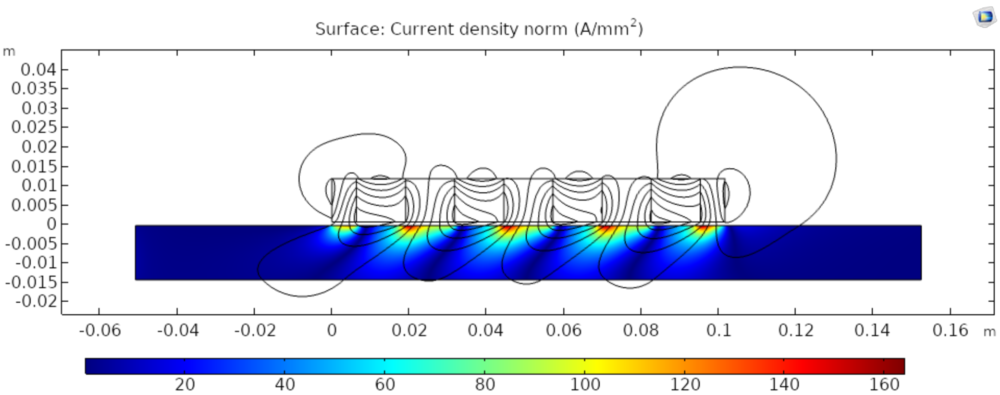

(c) Post/Arash best payload to drag

Figure 3.10: Eddy currents distribution within the track, $h_t = 14$mm

Therefore, they impose a lower bound on the distance between copper rim and PM array that shall be accounted for during tests. In particular, *Post/HTT single*

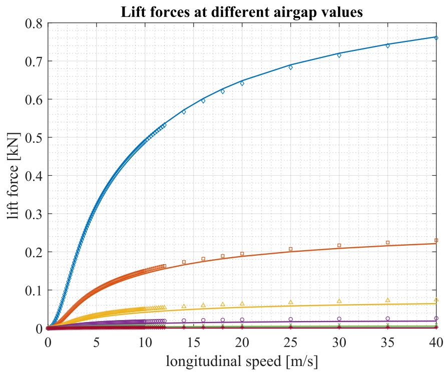

(a) Lift forces

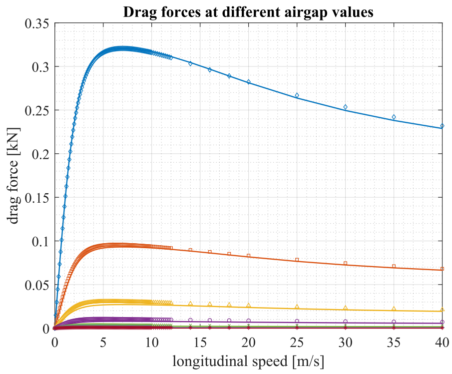

(b) Drag forces

Figure 3.11: Post/HTT single bogie

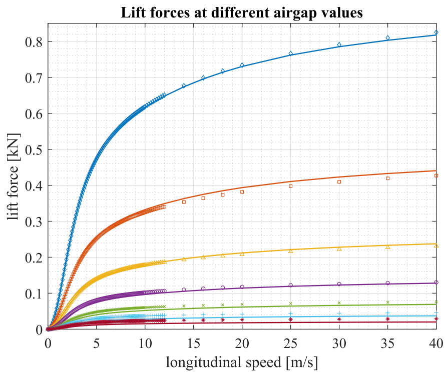

(a) Lift forces

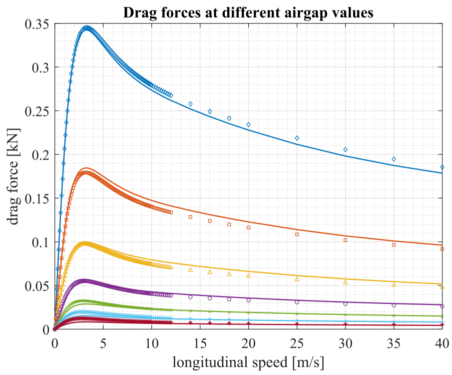

(b) Drag forces

Figure 3.12: Post/Alex single bogie

bogie configuration can be tested at airgap values strictly higher than 5mm, while *Post/Alex single bogie* arrangement guarantees $T < T_{max}$ for distances $z_p > 15mm$. No limiting values are retrieved for *Post/Arash best payload to drag* configuration, where the necessary torque and power to win the drag force are always lower than the motor's limits. The power and torque curves with respect to horizontal velocity and airgap can be found in Figures 3.14-3.16.

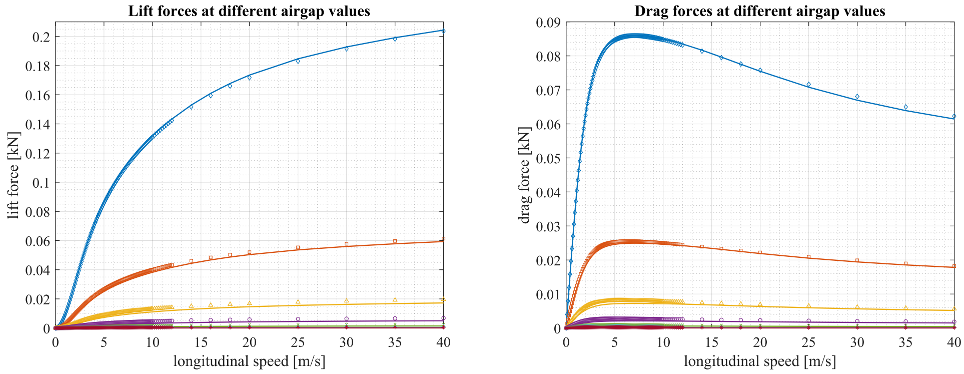

(a) Lift forces **(b)** Drag forces

Figure 3.13: Post/Arash best payload to drag

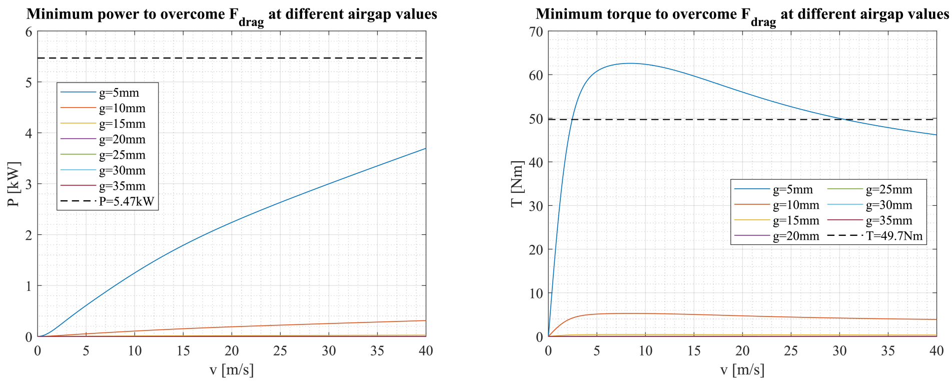

(a) Power to overcome F_D vs. P_{max} **(b)** Torque to overcome F_D vs. T_{max}

Figure 3.14: Post/HTT single bogie

3.4 Stability analysis and optimisation

This section summarises the results of numerical simulations of the dynamic behaviour of the levitation system. In this framework, the device is represented through a quarter car model, arranged as in Figure 2.6. The experiment will deal with vertical dynamics only, as described by Equation 3.10.

$$\begin{aligned}
\ddot{z}_p &= \frac{F_{\text{lift}}}{m_p} + \frac{c_s}{m_p}\left(\dot{z}_s - \dot{z}_p\right) + \frac{k_s}{m_p} z_s - \frac{k_s + k_{us}}{m_p} z_p - g \\
\ddot{z}_p &= -\frac{c_s}{m_s}\left(\dot{z}_s - \dot{z}_p\right) - \frac{k_s}{m_s}\left(z_s - z_p\right) - g
\end{aligned} \tag{3.10}$$

Here, lift force is described through the equivalent linear model. These relations are arranged in a state-space representation, whose state matrix A that can be

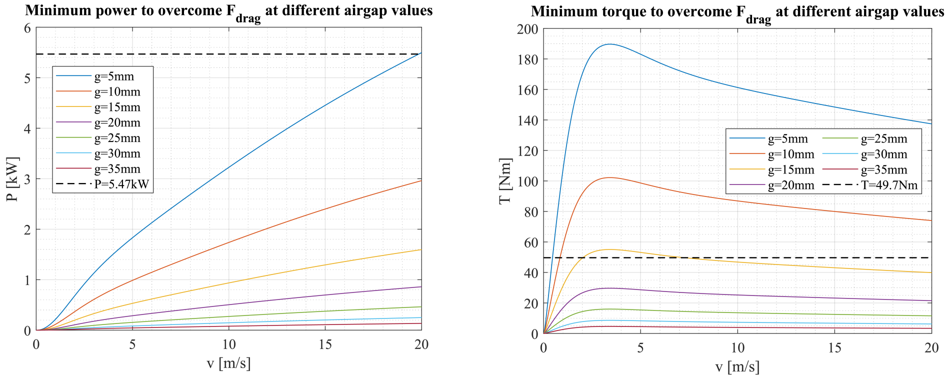

(a) Power to overcome F_D vs. P_{max} **(b)** Torque to overcome F_D vs. T_{max}

Figure 3.15: Post/Alex single bogie

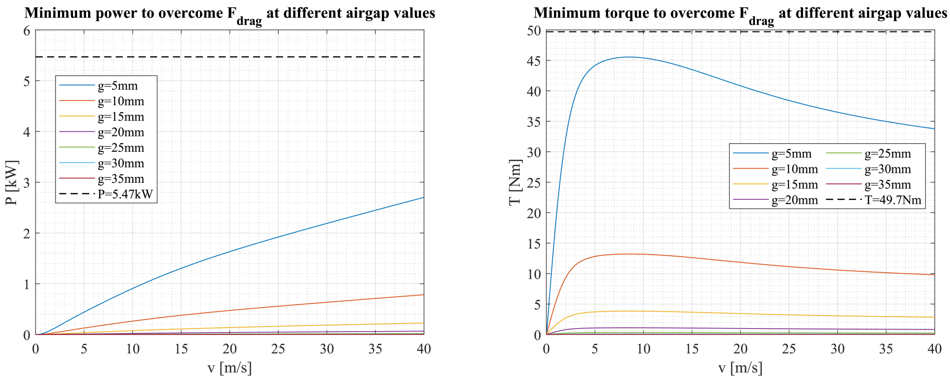

(a) Power to overcome F_D vs. P_{max} **(b)** Torque to overcome F_D vs. T_{max}

Figure 3.16: Post/Arash best payload to drag

found in Appendix A.

In order to properly identify the suspension damping that guarantees optimal stability conditions c_{opt}, the procedure described by Galluzzi et al. has been replicated. To this end, root locus analysis has been performed for different values of k_{us}: exploiting the description of the levitation system through its equivalent stiffness k_p [34, 33], the unsprung mass to stator spring has been swept in the range $(0 \div 0.1)k_p$. The results on the optimal damping and corresponding (minimum) real part of the most unstable pole are reported for $k_{us} = [0 \quad 0.05 \quad 0.1]k_p$ and for the three magnets arrangements in Table 3.9. One can notice that such minimum is achieved for the same value of c_s with negligible differences among the arrangements and as k_{us} varies. Therefore, a unique value of the optimal damping may be considered in the forthcoming design steps, and it may be approximated as:

$$c_{opt} = 250\,\mathrm{N\,s/m} \tag{3.11}$$

As an example, the complete evolution of the real part of the pole closest to the imaginary axis and damping ratio with respect to c_s is reported in Figures 3.17-3.19 for $k_{us} = 0.1k_p$ and for the three PM arrays to be tested.

		Post/HTT single bogie	Post/Alex single bogie	Post/Arash Best payload to drag
$k_{us} = 0k_p$	c_{opt}, Ns/m	249	249	249
	$\Re(p_i(c_{opt}))$	−6.42	−6.36	−6.4
$k_{us} = 0.05k_p$	c_{opt}, Ns/m	249	249	249
	$\Re(p_i(c_{opt}))$	−6.41	−6.35	−6.39
$k_{us} = 0.1k_p$	c_{opt}, Ns/m	249	249	249
	$\Re(p_i(c_{opt}))$	−6.4	−6.4	−6.38

Table 3.9: Optimal damping values and corresponding real part of the most unstable pole

Even when a downscaled system is considered, unstable behaviour can be observed for low damping values. Moreover, the real part of the most unstable pole has a global minimum which corresponds to the optimal damping value. When $c_s > c_{opt}$, poles merge onto the real axis, but the stability margin is reduced.

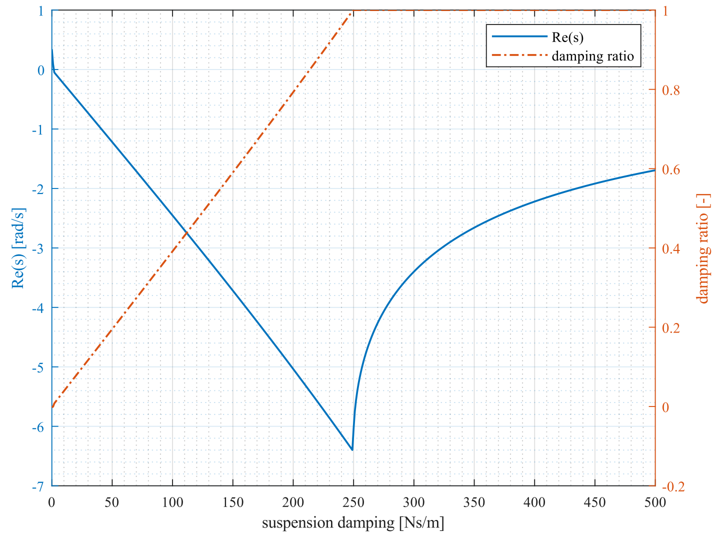

Figure 3.17: Stability optimisation, $k_{us} = 0.1k_p$. Post/HTT single bogie configuration

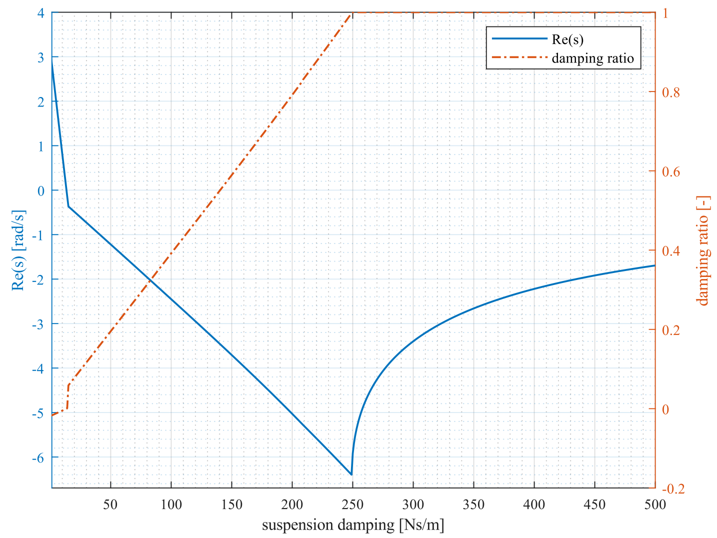

Figure 3.18: Stability optimisation, $k_{us} = 0.1k_p$. Post/Alex single bogie configuration

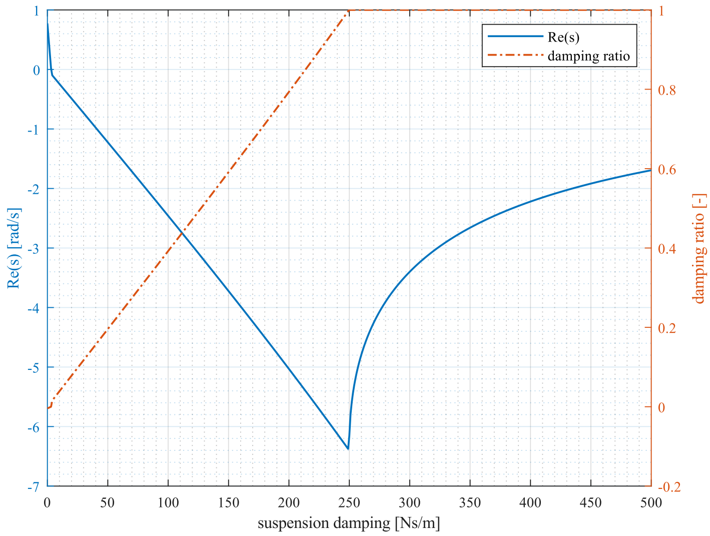

Figure 3.19: Stability optimisation, $k_{us} = 0.1k_p$. Post/Arash best payload to drag configuration

Chapter 4

Bearings selection

This chapter tackles the problem of bearing selection, whose main function consists in supporting the rotating shaft linked to the electric motor, that in turn allows rotation of the aluminium disk. The discussion is organised in three sections: at first, a worst case load evaluation procedure is carried out, by introducing relevant geometric parameters and physical phenomena. Afterwards, suitable devices are chosen, and their main features are summarised; the last section addresses the computation of bearings' frictional moment and power losses.

4.1 Problem formulation

Loads evaluation is carried out through dynamic equations and the free body diagram, whose reference geometry is the main frame layout in Figure 2.3. However, it is sufficient to consider the simplified structure in Figure 4.1, along with the following additional assumptions:

- the motor imparts a constant counterclockwise angular velocity $\Omega = 764$rpm on the shaft (that corresponds to the maximum allowable peripheral speed $v = 40$m/s);
- the shaft has a negligible mass $m_{sh} \approx 0$ with respect to that of the disk M.

4.1.1 Evaluation of unbalance force and momentum

In order to properly carry out the dynamic analysis, additional quantities that account for unbalance forces shall be considered. Given the non negligible moment of inertia of the disk, the examined case study can be assimilated to a multi-degree of freedom rotor[35].

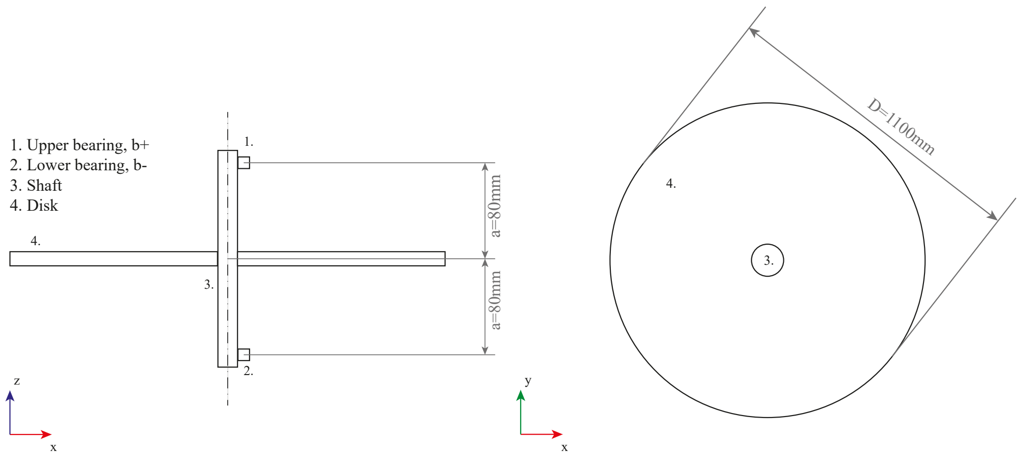

(a) xz plane **(b)** xy plane

Figure 4.1: Test bench: shaft, bearings and disk, simplified layout

In particular, the static and couple unbalance (unbalance force and momentum respectively) are due to the non zero distance between the centre of the shaft and the centre of mass of the rigid body, **eccentricity** ε, and to the non null angle χ between the symmetry axis and the rotation axis.

The static unbalance can be quantified by means of the **quality grade for balancing**, defined as:

$$G = \Omega\varepsilon \tag{4.1}$$

Possible values in mm/s for this parameters are suggested by the ISO 21940-11 standard [36] according to the type of rotor and application.
In this framework, a suitable value can be $G = 6.3$mm/s, thus yielding:

$$\varepsilon = \frac{G}{\Omega} \approx 0.079\text{mm} \tag{4.2}$$

Afterwards, the amplitude of the unbalance terms may be computed as:

$$F_{unb} = M\Omega^2\varepsilon = 50.40\text{N} \tag{4.3}$$

$$M_{unb} = F_{unb}a = 4.03\text{Nm} \tag{4.4}$$

while their expression as a function of time is that of a harmonic function:

$$F_u(t) = F_{unb}\cos(\Omega t + \phi_F) \tag{4.5}$$

$$M_u(t) = M_{unb}\sin(\Omega t + \phi_M) \tag{4.6}$$

4.1.2 Free body diagram and derivation of bearing reactions

Afterwards, force and momentum equilibria along the axes are written according to the free body diagrams in Appendix B.2. The equations are solved for the components of reactions on the bearings along the x, y and z axes, as highlighted in Equation 4.7, where $g = 9.81\text{m/s}^2$ is the gravity acceleration.

$$\begin{aligned}
F_{b+,x} &= \frac{F_u(t)}{2} + \frac{\frac{F_{lift}D}{2} + M_u(t)}{2a} \quad & F_{b-,x} &= \frac{F_u(t)}{2} - \frac{\frac{F_{lift}D}{2} + M_u(t)}{2a} \\
F_{b+,y} &= \frac{F_u(t) - F_{drag}}{2} - \frac{M_u(t)}{2a} \quad & F_{b-,y} &= \frac{F_u(t) - F_{drag}}{2} + \frac{M_u(t)}{2a} \\
F_{b+,z} &= \frac{F_{lift} + Mg}{2} = 0.56\text{kN} \quad & F_{b-,z} &= \frac{F_{lift} + Mg}{2} = 0.56\text{kN}
\end{aligned} \tag{4.7}$$

Assuming $\phi_F = \phi_M = 0°$, the time evolution (Figure 4.2) of said loads have been evaluated to assess their maximum absolute values and amplitude, reported in Table 4.1. To this end the worst case scenario is also assumed as far as electromagnetic lift and drag forces are concerned: maximum F_{lift} and F_{drag} among the three different magnet arrangements and are reported in Equation 4.8.

$$F_{lift} = 228.1\text{N} \qquad F_{drag} = 90.37\text{N} \tag{4.8}$$

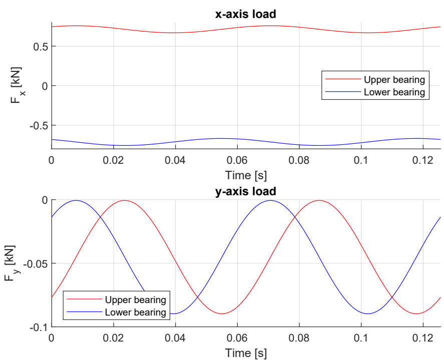

Figure 4.2: Time evolution of loads component over x and y axes.

Max. absolute value, $[kN]$			
	F_{bx}	F_{by}	F_{bz}
Upper bearing	0.75	0.08	0.6
Lower bearing	0.75	0.08	0.6
Amp. of alternating load, $[kN]$			
	F_{bx}	F_{by}	F_{bz}
Upper bearing	0.036	0.036	0
Lower bearing	0.036	0.036	0

Table 4.1: Bearing loads components over the Cartesian axes.

4.2 Item selection

The choice of suitable bearings in terms of static and fatigue safety factor, as well as housing dimensions has been carried out through the online tool *SKF Bearing Select*, provided by the company SKF®. This helps the designer in finding the most appropriate device within its catalogue[37], exploiting all the available information.

In order for the choice to be sufficiently conservative, loads are multiplied by a coefficient equal to 3, thus yielding the maximum absolute values in Table 4.2.

	F_{bx}	F_{by}	F_{bz}
Upper bearing	2.25kN	0.24kN	1.8kN
Lower bearing	2.25kN	0.24kN	1.8kN

Table 4.2: Maximum absolute value of loads on bearings along the three Cartesian axes

4.2.1 Features

Bearing type and principal dimensions

Given the presence of both radial and axial loads, suitable support can be provided by angular contact ball bearings. An important advantage provided by such configuration can be the small contact surface between rolling elements and inner ring, that yields low friction losses.
Assuming an inner shaft diameter $d = 30$mm, the selection tools suggests as a possible solution, the item **7206 BECBP** (datasheet in Ref. [37]), whose principal dimensions and ratings are reported in Table 4.3.

Principal dimensions		
Bore diameter d	Outer ring diameter D	Width B
30mm	62mm	16mm
Load ratings		
Dynamic C	Static C_0	Fatigue limit P_u
24kN	15.6kN	0.655kN

Table 4.3: Dimensions and load ratings of SKF7206 BECBP angular contact ball bearings.

Rating life evaluation

According to the ISO 281 standard[38], the basic rating life of a bearing (at 90% reliability) measured in millions of cycles is computed as:

$$L_{10} = \left(\frac{C}{P}\right)^p \tag{4.9}$$

where $p = 3$ (for ball bearings) is the exponent of the life equation, C is the basic dynamic load rating, specific for each device, P is the equivalent dynamic bearing load. It is defined as $P = X \cdot F_r + Y \cdot F_a$, where X and Y are tabled coefficients, $F_r = \sqrt{F_{bx}^2 + F_{by}^2}$ is the radial force, and $F_a = F_{bz}$ is the axial force. Here, $P = 2.47$kN on the upper bearing, $P = 3.96$kN on the lower bearing.

Given the need to account for the lubrication and contamination levels of the bearing and the fatigue limit of the material, a life modification factor a_{SKF} can be introduced for an alternative life estimation. Its value depends on the lubricant conditions and contamination conditions. A further factor a_1 adjusts reliability.

$$L_{nm} = a_1(n) a_{SKF} L_{10} \tag{4.10}$$

Here, n is the failure probability upon which a_1 is selected.

The values of the above mentioned parameters for the analysed application are reported in table 4.4.

	Basic rating life L_{10h}	SKF rating life L_{10mh}	SKF life modification factor a_{SKF}
b_+	20000 h	46400 h	2.32
b_-	4840 h	6600 h	1.36

Table 4.4: Bearing life evaluations

Loads and static safety

The static safety factor s_0 is evaluated as in Equation 4.11, where C_0 is the static load rating, and $P_0 = X_0 \cdot F_r + Y_0 \cdot F_a$ is the equivalent static load. It is equal to 6.32 for the upper bearing and to 6.01 for the lower one, thus ensuring correct operation.

$$s_0 = \frac{C_0}{P_0} \tag{4.11}$$

Lubrication

A general purpose industrial grease has been selected as lubricant. Viscosity parameters are reported in Table 4.5. There, ν is the actual operating viscosity of the grease, determined through its ISO viscosity grade and operating temperature, ν_1 is the rated viscosity, which varies with the mean bearing diameter and its rotational speed. The lubrication condition of the bearing is given by its viscosity ratio $\kappa = \frac{\nu}{\nu_1}$.

	ν, mm^2/s	ν_1, mm^2/s	κ
b_+	28.0	22.0	1.26
b_-	28.0	22.0	1.26

Table 4.5: Viscosity data

The selection tool suggests a grease quantity equal to 5g per bearing, and a re-lubrication interval equal to 6060h (upper bearing) and 3440h (lower bearing), for a suitable contamination level.

4.2.2 Fits and tolerances

The load case examined requires interference fit both on the shaft and on the bearing housing. The tolerance classes as in ISO 286-2[39] are h6 and N7 respectively.

4.3 Friction and power losses

It is useful to identify frictional moment and power losses on the bearings. Given the complexity of the phenomenon that involves the lubricant film between the rolling elements, raceways and cages, the computation of these quantities has been demanded to the selection tools.

The SKF® model describes frictional moment as a sum of four contributions.

$$M = M_{rr} + M_{sl} + M_{seal} + M_{drag} \qquad [M] = \mathrm{N\,mm} \tag{4.12}$$

where:

- M_{rr} is the rolling frictional moment, that accounts for possible lubricant shortage;
- M_{sl} is the sliding frictional moment, that includes the effects of lubricant quality;
- M_{seal} that accounts for friction within seals;
- M_{drag} that accounts for friction phenomena related to oil-based lubrication.

Another meaningful parameter is the starting torque M_{start}, that accounts for the torque to be overcome by the bearings to start rotating at ambient temperature. Its expression is:

$$M_{start} = M_{sl}(T_{amb}) + M_{seal}(T_{amb}) \tag{4.13}$$

Given M, power losses are evaluated as:

$$P_{loss} = 1.05 \cdot 10^{-4} \Omega M \tag{4.14}$$

The above described quantities are reported in Table 4.6.

	M	M_{start}	M_{rr}	M_{sl}	M_{seal}	M_{drag}	P_{loss}
						Nmm	W
b_+	128	246	22.2	106	0	0	10
b_-	262	504	45.7	217	0	0	21

Table 4.6: Friction and power losses

Chapter 5

Suspension design

This chapter deals with the preliminary steps of the secondary suspension design and control and it is further organised in two sections. The former addresses the description of the target output force, and provides motivations on the use of a voice coil actuator to achieve the above mentioned control objectives; furthermore, an overview on the principle of operation of VCAs is reported, along with the main characteristics of the physical device chosen to implement the suspension. The second section discusses possible control strategies in the Linear Time Invariant systems framework, pointing out a preliminary architecture, relevant signals and necessary sensors, control law structure, as well as advantages and disadvantages of each.

5.1 Problem statement

The root locus analysis in Section 3.4 points out the existence of a optimal damping value c_{opt} that guarantees the best possible stability margins, hence the need for an additional suspension, as already highlighted in *Galluzzi et al.* [8]. Moreover, given the low stiffness value k_s for the spring between the unsprung and sprung mass, the need arises to compensate the static deformation on the elastic connections due to the weight of the sprung mass. This is fundamental to ensure the operation of such devices within their linear region.

Therefore, the suspension between the sprung and unsprung mass shall provide the system with two force contributions, as shown in Equation 5.1. Here, F_d depends on the relative velocity $v = \dot{z}_s - \dot{z}_p$ and yields the required damping, while F_w accounts for static deformation compensation and it is a function of the relative displacement $z_s - z_p$.

$$F_s = F_d + F_w = f\left(\dot{z}_s - \dot{z}_p\right) + g\left(z_s - z_p\right) \tag{5.1}$$

5.1.1 Voice coil actuators: an overview. Device selection

To fulfil these objectives, one can make use of classic viscous dampers. However, both oil and elastomers based devices shall be employed only after an accurate thermal analysis has assessed the feasibility of the application: these devices can in fact be subject to an uncontrolled and unstable temperature increase, due to energy dissipation as heat, that may yield irreversible damages [35]. An alternative solution that does not need the above mentioned additional studies and yields higher precision and flexibility in control consists in employing a voice coil. It is a type of electromagnetic linear actuator, whose schematic representation on a conceptual level may be found in Figure 5.1. Such item is composed of a magnetic circuit in which a conductive coil is immersed; relative vertical displacement between these parts is allowed, so that the solenoid is subject to Lorentz force.

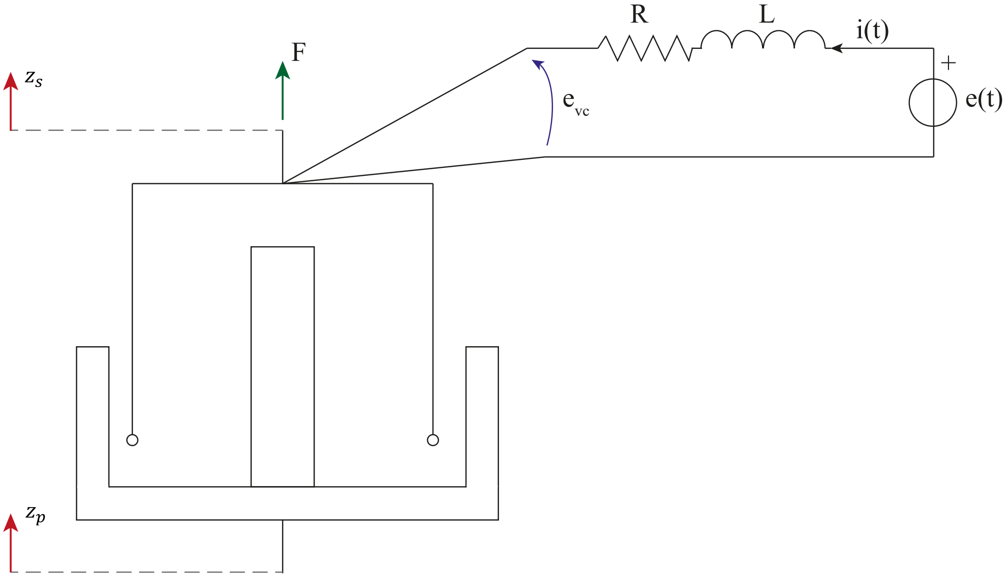

Figure 5.1: Voice coil scheme

Constitutive relations for the device can be found in Equation 5.2. The constant $K_m = 2\pi BrN$ accounts for the magnetic field $\vec{B}$ and for the coil geometry through its average radius r and number of windings N. In the electrical domain, one can write a Kirchhoff voltage law to relate the relative velocity between the coil and permanent magnet with the voltage $e(t)$ and current $i(t)$ that flow through the solenoid, by means of the same constant K_m and the parasitic inductance L and resistance R, here considered as lumped parameters.

$$\begin{aligned} F(t) &= K_m i(t) \\ e(t) &= L\frac{\mathrm{d}i(t)}{\mathrm{d}t} + Ri(t) + k_m v(t) \end{aligned} \tag{5.2}$$

The force-velocity transfer function reported in Equation 5.3 defines a variable damping, upon which one can act through automatic control techniques. Its steady state gain $c_{ss} = \frac{K_m^2}{R}$ provides a reference parameter to be used for the device selection, since the relation $c_{ss} > c_{opt}$ must be valid.

$$c_{VC}(s) = \frac{F(s)}{v(s)} = -\frac{K_m^2}{sL + R} \tag{5.3}$$

To this end, a feasible implementation may be performed through the commercial item VM108-2P30-1000 by Geeplus™(datasheet at Ref. [40]), whose main features are reported in Table 5.1. In particular, its nominal steady state damping is equal to 481Ns/m, thus being compliant with the above mentioned requirement. Moreover, the maximum continuous force is larger than the weight of the sprung mass, thus allowing some margin to implement F_d.

Description	Expression	Value	Unit
Resistance	R	1.3	Ω
Inductance	L	N.A.	H
Force constant	K_m	25	N/A
Maximum output current	I_{max}	7.7	A
Peak force	F_{max}	230	N
Total mass	M_{TOT}	8	kg
Coil mass	m_c	0.75	kg

Table 5.1: Voice coil actuator VM108-2P30-1000, physical parameters

5.2 Possible control strategies

On the basis of the linearisation performed in Section 3.3, the whole system under study may be considered LTI. Therefore, the superposition principle may be applied to meet the above mentioned requirements as two separate contributions; this task may be performed by adopting different architectures, that are described in the forthcoming subsections.

5.2.1 Static current feedback with feedforward weight compensation

The simplest strategy employs the voltage $e(t)$ as control input.

1. Damping is tuned through a static state feedback law. When $e_d(t) = -\alpha i(t)$, $\alpha \in \mathbb{R}$ is substituted in Equation 5.2, the Laplace domain expression that

relates the velocity $v(t)$ with the output force $F(t)$ is the real rational function in Equation 5.4.

$$\frac{F(s)}{v(s)} = \frac{-k_m^2}{sL + (R+\alpha)} \tag{5.4}$$

The expression of the transfer function is that of a frequency dependent damping. Therefore, the real parameter α is tuned to obtain a steady-state gain equal to c_{opt}, as highlighted in equation 5.5.

$$\alpha \,\text{s.t.}\ \lim_{s\to 0}\left|\frac{F(s)}{v(s)}\right| = \frac{k_m^2}{R+\alpha} = c_{opt} \tag{5.5}$$

2. The weight of the sprung mass, $W_s = m_s g$, is instead compensated through a constant force offset. In the electrical domain, such quantity is a constant voltage. Its expression can be derived by writing a static relation among the voice coil physical quantities, as reported in Equation 5.6.

$$\begin{cases} e = (R+\alpha)i \\ F = k_m i \end{cases} \quad \Rightarrow \quad e_w = \frac{P}{k_m}(R+\alpha) = \frac{m_s g}{k_m}(R+\alpha) \tag{5.6}$$

As a consequence, the complete control law can be read in Equation 5.7, while the system architecture is reported in Figure 5.2.

$$e(t) = e_d(t) + e_w(t) = -\alpha i(t) + \frac{m_s g}{k_m}(R+\alpha) \tag{5.7}$$

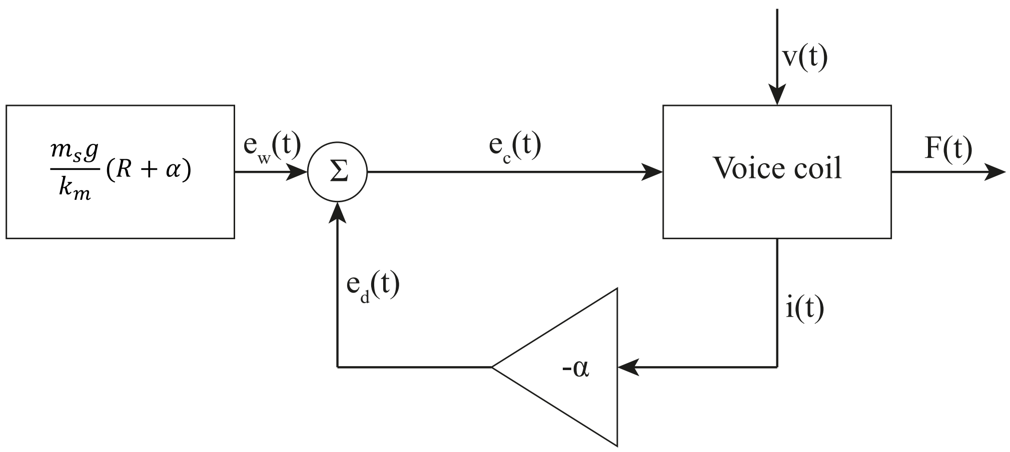

Figure 5.2: Voice coil control architecture: voltage feedback with constant weight compensation

5.2.2 Current feedback with proportional-integral controller

This model, however, has poor accuracy properties as far as weight tracking and noise rejection are concerned. In fact, e_w is tuned a priori and with a feedforward architecture: this could hinder the achievement of the control purpose thus causing undesired phenomena during the experiment. A simple yet important improvement can be performed when the structure in Figure 5.3 is employed.

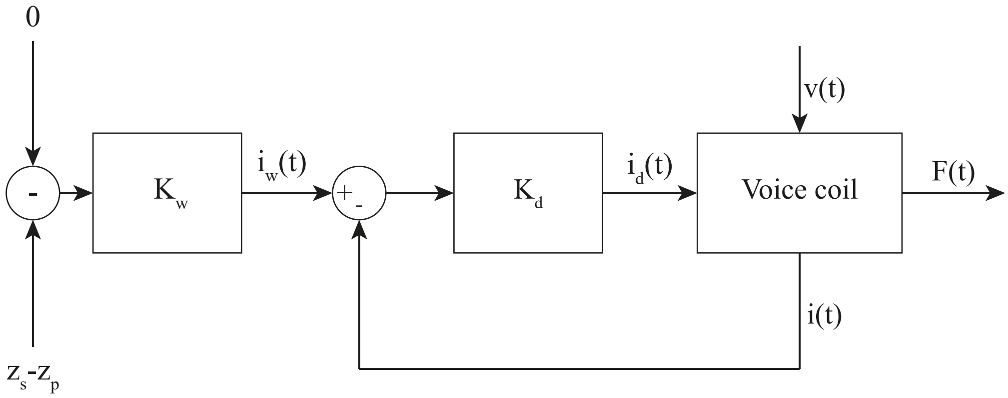

Figure 5.3: Voice coil control architecture: current feedback with zero regulation of $z_s - z_p$

Here, the PI controller $K_w(s)$, regulates to 0 the static deformation $z_s - z_p$ of the elastic connections, that is measured through position sensors on the sprung and unsprung mass. This element also performs the necessary unit conversion from position to force to the current $i_w(t)$, which act as a reference signal for the forthcoming stage.

In order to obtain the optimal damping value, the voice coil current is tuned by means of the additional PI controller $K_d(s)$. This architecture is fully functional when $K_w(s)$ and $K_d(s)$ have separate bandwidths. In particular, since position regulation shall be performed at steady-state only, a possible solution features a narrow bandwidth for $K_w(s)$, so that the current loop can act at medium frequencies.

5.2.3 Current feedback with proportional-integral controller and velocity estimation

Further accuracy in tracking can be achieved when a damping force reference is provided to the current loop. A possible implementation is proposed in Figure 5.4, and it employs both position and acceleration sensors.

In particular, the reference signal to the current loop is here composed of two contributions:

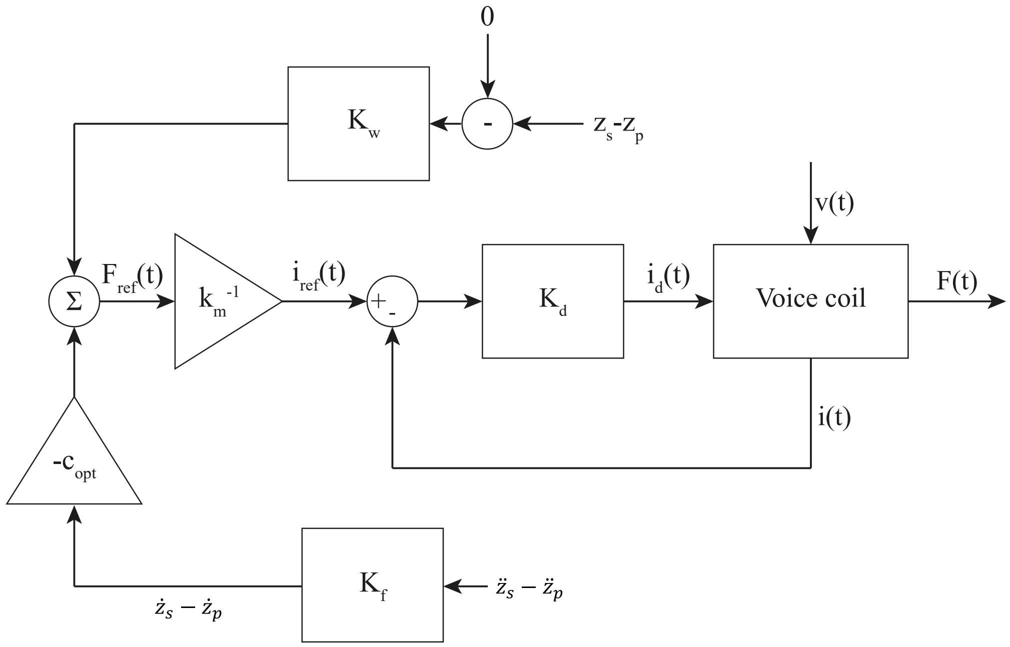

Figure 5.4: Voice coil control architecture: current feedback with zero regulation of $z_s - z_p$ and $\dot{z}_s - \dot{z}_p$ reference

- $i_w(t) = \frac{F_w(t)}{k_m}$ that accounts for zero regulation of static deformations of k_s;
- $i_c(t) = \frac{F_c(t)}{k_m}$ that is the desired damping force value, computed when the relative velocity $\dot{z}_s - \dot{z}_p$ between sprung and unsprung mass is extracted from acceleration data through the Kalman filter $K_f(s)$.

In addition to the highest possible accuracy in terms of reference tracking, this solution provides a suitable noise rejection level due to the implementation of $K_f(s)$. The design of the PI controllers $K_w(s)$ and $K_d(s)$ can be performed with the specifications mentioned for the previously described structure.

Chapter 6

Experiments procedure and functional tests results

In this chapter the complete experiments course of action is analysed and discussed. Moreover, preliminary results in the suspension control framework are presented: in particular, software simulations have been run on the three proposed control strategies. Afterwards, the outcome of functional tests on the target hardware device to be used as MCU are discussed. It is worthwhile noticing that, since the actual test bench hasn't been assembled yet, the performed functional tests assess the behaviour of the simplest suspension design control strategy only: when the velocity estimation solution is considered, an actual mechanical interface is instead necessary. Both simulations and tests have been run on the basis of the *model-based* design methodology[41].

6.1 Activity course of action

The experimental validation of the models proposed in Chapters 3 to 5 is aimed at assessing both the validity of the mathematical characterisation of the levitation device (in terms of linear lumped parameters model and by rigorously retrieving its unstable behaviour), as well as the feasibility of the proposed stabilisation strategies. In order to replicate as much as possible the modelling assumptions, so as to avoid cross-coupling between different physical phenomena, which could deteriorate data readability, experiments are performed in different frameworks, as described in Chapter 2.

In particular, the system identification procedure relies on lift and drag forces data collected in quasi-static conditions, that are measured by means of the system described in Section 2.2; the complete test procedure consists in three main phases.

1. The relative distance between the pad and the copper runaway is imposed by means of the micrometric linear stage (see Figure 2.4). Afterwards, the electric motor drives the disk to the target rotational speed which yields the desired longitudinal velocity between the track and the bogie.

2. Lift and drag forces are measured for constant airgap z_p and velocity v_{in} by means of load cells. This procedure is repeated over the airgap and speed ranges.

3. On the basis of measurements results, model parameters are estimated: the optimal number of branches N_b yields values of the pole frequencies $\omega_{p,k}$ and inductances L_k.

Stability properties of the levitation device shall, instead, be assessed in a dynamic framework, since relative vertical displacement between the bogie and the track shall be allowed. To this end, the measurement system described in Section 2.3 is employed. The test is carried out by means of the following steps.

1. An initial value for the airgap z_p, close to the expected steady-state distance, is set through the micrometric linear stage. Therefore, the target rotational angular velocity is imparted on the disk.

2. The dynamic behaviour of the system is evaluated through the evolution of the airgap z_p and the sprung mass acceleration $\ddot{z}_s$, measured by means of position and velocity sensors. Such assessment is repeated for different damping values.

6.2 Model-in-the-loop tests

The first step towards the development of experimental results consists in *model-in-the-loop* (henceforth, MIL) simulations. Here, both the physical system and the controller are represented as mathematical entities, and their interconnection is purely ideal[]. However, at this stage one shall model the analogue to digital and digital to analogue conversion phenomena, in order to assess the validity of the interaction between the continuous time domain of the levitation device, and the discrete time framework in which the controller is implemented. The experiment is entirely simulated on a PC through the *Mathworks*®software *Simulink*.

The target damping c_{des} plays the role of the reference signal, that is properly conditioned and provided to the control algorithm. Therefore, the interaction between the controller's output, the voice coil actuator and the plant may be represented as in Figure 6.1: the voltage e_c drives the VCA, which in turns provides the mechanical subsystem (i.e. quarter-car model) with the desired force F_{VC}. An additional input to this domain is the electrodynamic lift force, that is the result of the interaction between the permanent magnets array and the copper rim. Furthermore, a separate subsystem features the statement of the input horizontal velocity v_{in} generated by the electric motor, and it allows to define perturbations on the vertical displacement of the levitation device, so that the effects of airgap variations may be studied.

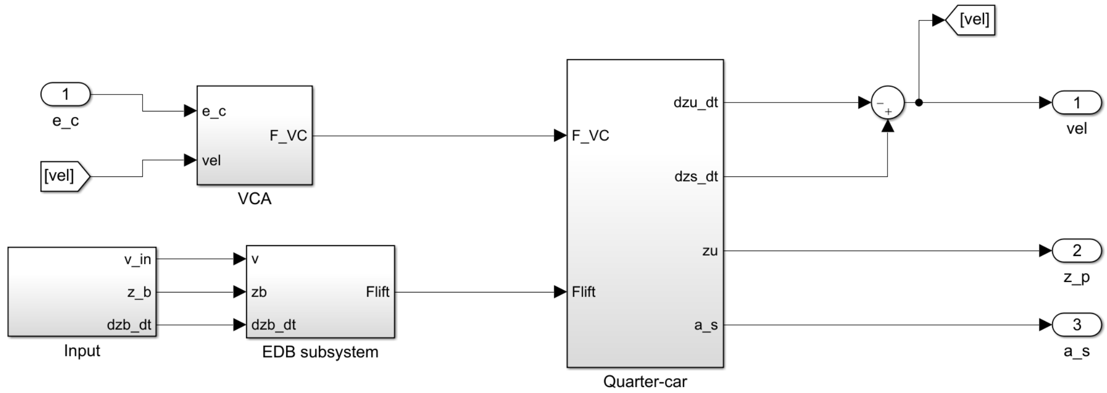

Figure 6.1: Plant and actuator, Simulink®model

6.2.1 Speed profile evaluation

In order to provide more realistic simulation outcomes, it is necessary to design a trapezoidal longitudinal speed profile that accounts for motor's power on and power off stages, and that features a steady-state sector corresponding to the target speed v. However, in order to impart angular velocity on the disk, the motor must overcome a resistant torque, that is the result of several contributions. Among those, the most relevant is the electromagnetic friction generated by the drag force F_D and its associated momentum M_D; on the same plane, bearings frictional moment M_b computed in Section 4.3 takes place. In this analysis, air resistance and power losses occurring in the shaft and in the torsional joint (see Figure 2.3) are neglected. Therefore, Newton's second law for rotation in Equation 6.1 is written, with respect to the centre of the disk O, on the basis of the free body diagram in Figure 6.2; given I_D inertia of the rotating disk, M_D and M_b, the angular acceleration $\dot{\omega}$ is a design variable that can be chosen in a way that the torque T_M provided by the motor doesn't exceed its maximum continuous value T_{max}.

$$I\dot{\omega} = T_M - M_D - M_b \quad \Rightarrow \quad T_M = I\dot{\omega} + M_D + M_b \leq T_{max} \tag{6.1}$$

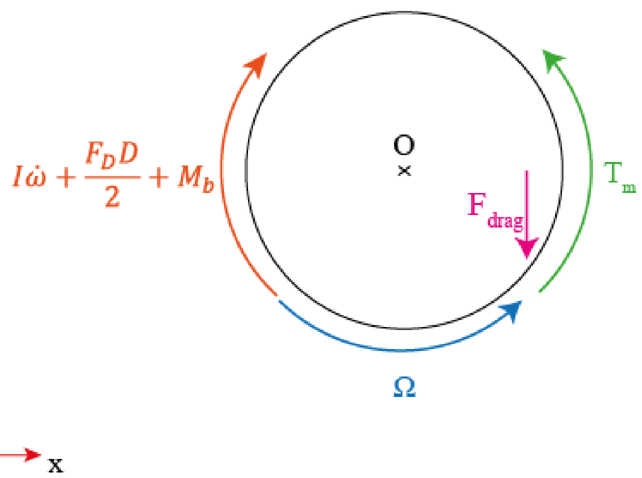

Figure 6.2: Disk free body diagram

The selected longitudinal speed v_{in} is reported, for the three magnets configurations under study, along with the resulting resistant torque and unsprung mass position profile in Figures 6.3-6.5. In particular, the steady-state velocity value has been increased to 50m/s, since the previously selected value of 40m/s yielded sub-optimal results when dealing with Post/HTT single bogie configuration. Such increase of the target relative velocity between the track and the capsule does not require further design adjustments as far as mechanical design or motor's limiting angular speed are concerned, and it is beneficial in terms of drag force, which decreases with higher values of v_{in}. However, bearings loads undergo some changes, which in turn leads to variation in the frictional moment; relevant parameters concerning this new scenario can be read in Table 6.1.

	Maximum absolute loads			Frictional moment		Power loss
	F_x	F_y	F_z	M	M_{start}	P_{loss}
			kN		Nmm	W
Upper bearing b_+	2.27	0.27	0.81	124	254	12
Lower bearing b_-	2.27	0.27	0.81	262	538	36

Table 6.1: Bearings load case, frictional moment and power losses when $v_{in} = v = 50\text{m/s} \rightarrow \omega = \Omega = 955\text{rpm}$

These results suggest that when the relative velocity is too low, and the lift force is unable to counteract the weight of the capsule, the effect of the electrodynamic drag are predominant and they overcome by a large amount the maximum allowable torque T_{max}. Moreover, neither the effect of the slope of the speed profile (namely,

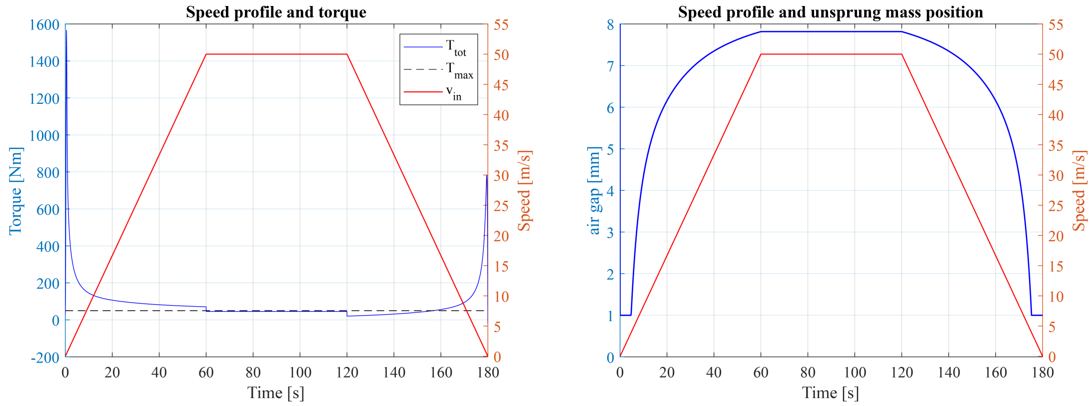

(a) Total resistant torque vs. maximum torque with respect to the input speed profile

(b) Unsprung mass position with respect to the input speed profile

Figure 6.3: Post/HTT single bogie configuration

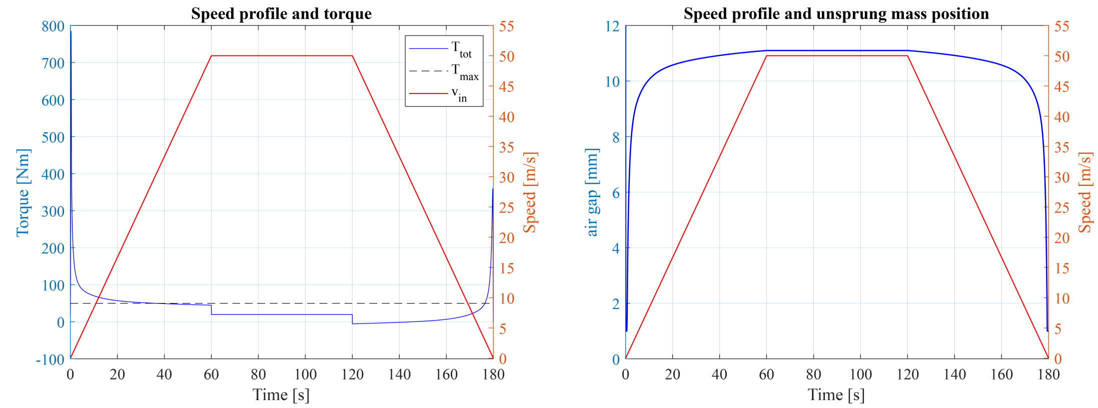

(a) Total resistant torque vs. maximum torque with respect to the input speed profile

(b) Unsprung mass position with respect to the input speed profile

Figure 6.4: Post/Alex single bogie configuration

the acceleration $\dot{v}_{in} = \dot{\omega}\frac{D}{2}$) nor bearings frictional moment provide a significant influence on this phenomenon. In the full-scale *Hyperloop* system, the trains will be equipped with wheels that shall be able to provide both the necessary speed through the airgap transient, and a safety mechanism in case of system failure [4]. Hence the need for a structure that is capable of maintaining a sufficiently large airgap value, which in turn yields a low enough drag force throughout the whole duration of the test. In the analysed test framework, such condition can be

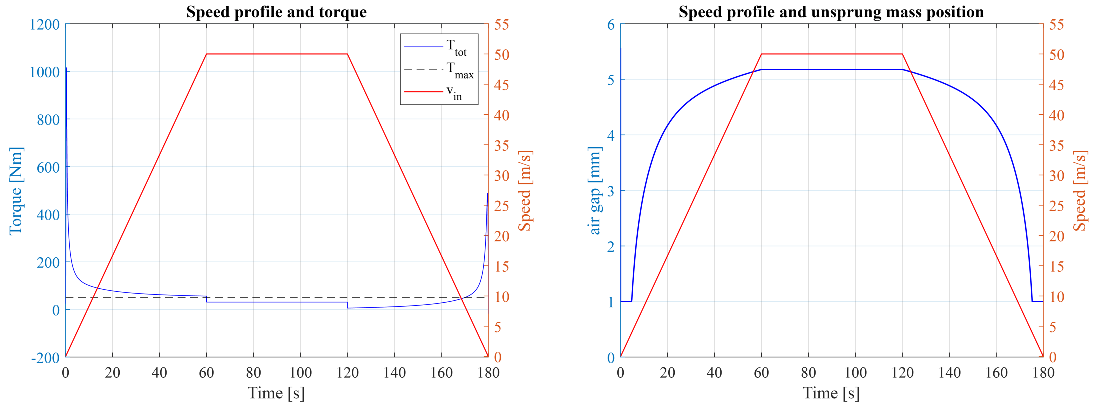

(a) Total resistant torque vs. maximum torque with respect to the input speed profile

(b) Unsprung mass position with respect to the input speed profile

Figure 6.5: Post/Arash best payload to drag configuration

achieved by including limit switches in the micrometric linear stage, that serves as a stator (see Figure 2.5), in order to guarantee a suitable minimum distance from the track. The load case study and the design of this component are, however, outside the scope of this thesis. However, in the forthcoming analysis, the airgap z_p has been allowed to oscillate for a 2mm wide range centred around its steady-state equilibrium value.

6.2.2 Current feedback and feedforward weight compensation

The simplest solution to the suspension control problem, consists in adjusting the total coil resistance to the value that yields the target damping, and in adding the weight compensation term as a constant voltage offset. A possible architecture has been discussed in Section 5.2.1. Simulations have been performed for two different damping values, the optimal $c_{des} = c_{opt} = 250Ns/m$, and a much lower value $c'_{des} = 10Ns/m$. Control parameters are reported in Table 6.2, while results in terms of force tracking, command input and output signal monitoring are shown in Figures 6.6, 6.7 and 6.8 respectively. The time axis has been resized to better inspect the transient behaviour of the above mentioned signals.

At a glance, the effect of selecting a low target damping is self evident: even though it does not yield instability, the amplitude of the oscillations and their settling time is much higher than the case in which $c_{des} = c_{opt}$. Furthermore, the maximum control voltage required to stabilise the system is equal to $e_{c,max} \approx 420$V, which is not compliant with the limitations of the DC bus that shall be used to

Target damping	α	e_w
$c_{des} = 250Ns/m$	1.2Ω	16.68V
$c_{des} = 10Ns/m$	61.2Ω	416.93V

Table 6.2: Controller parameters: current feedback and feedforward weight compensation

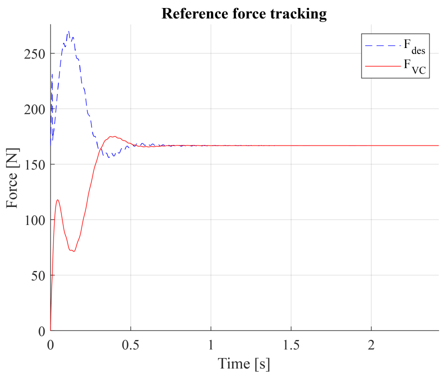

(a) $c_{des} = 250Ns/m$

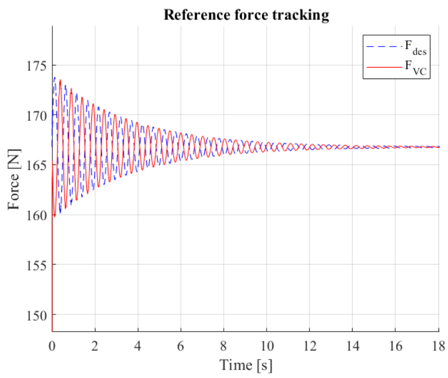

(b) $c_{des} = 10Ns/m$

Figure 6.6: Desired force at VCA output: reference tracking

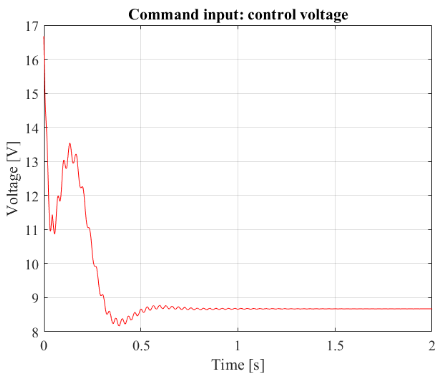

(a) $c_{des} = 250Ns/m$

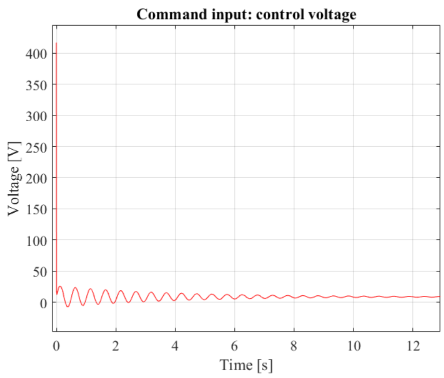

(b) $c_{des} = 10Ns/m$

Figure 6.7: Command input: control voltage

drive the VCA.
As far as the performances of the control system are concerned, it shows poor properties in terms of transient tracking, while the steady state desired force requirement is met. However, given the absence of transient requirements such as maximum overshoot, rise and settling time, this aspect has minimal influence on the course of the experiment. A key role is played by the Furthermore, its

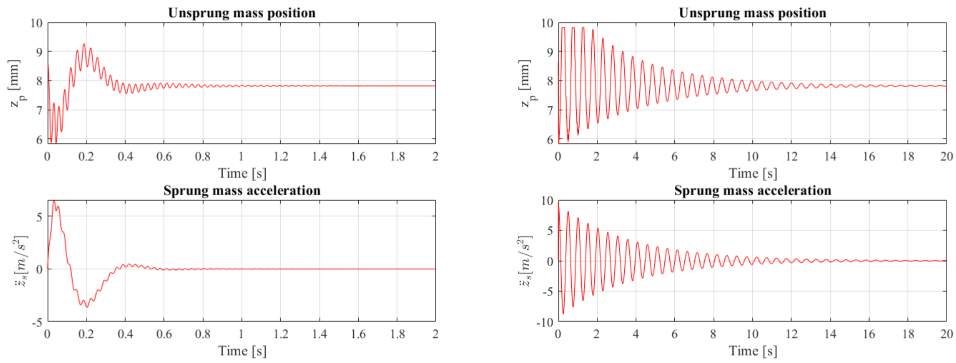

(a) $c_{des} = 250Ns/m$ **(b)** $c_{des} = 10Ns/m$

Figure 6.8: Output signals monitoring: unsprung mass position and sprung mass acceleration

intrinsically simple architecture and implementation make this solution feasible for functional tests and preliminary assessments on the test bench. However, ringing phenomena are observed in the control output e_c: this is particularly undesirable, since it would yield additional current flow within the electrical port of the VCA, which can in turn cause overheating of the device.

6.2.3 Current feedback with proportional-integral controller

An improvement to the above discussed solution is the architecture in Figure 5.3, since it provides the designer with an additional degree of freedom, that is the integral gain, which can improve the dynamics of the closed loop system. However, said structure is not able to stabilise the device *per se*, since a damping force reference is not provided; furthermore, position regulation techniques were not able to extract the weight term. As a consequence, a more suitable structure is reported in Figure 6.9.
The proportional-integral controller is implemented as a discrete time transfer function that can be read in Equation 6.2, where the sampling time T_s has been set to $5 \cdot 10^{-5}$s.

$$C_{PI}(z) = P + I \cdot T_s \frac{z}{z-1} \tag{6.2}$$

The real coefficients P and I can be tuned to ensure, respectively, proper settling time and zero steady-state tracking error[42]. The derivative action is here not considered, since in general it induces high frequency oscillations on the control input, that shall instead be avoided.

Here, controller coefficients have been set through a trial and error procedure. Two relevant design steps and related simulation outcomes are summarised through

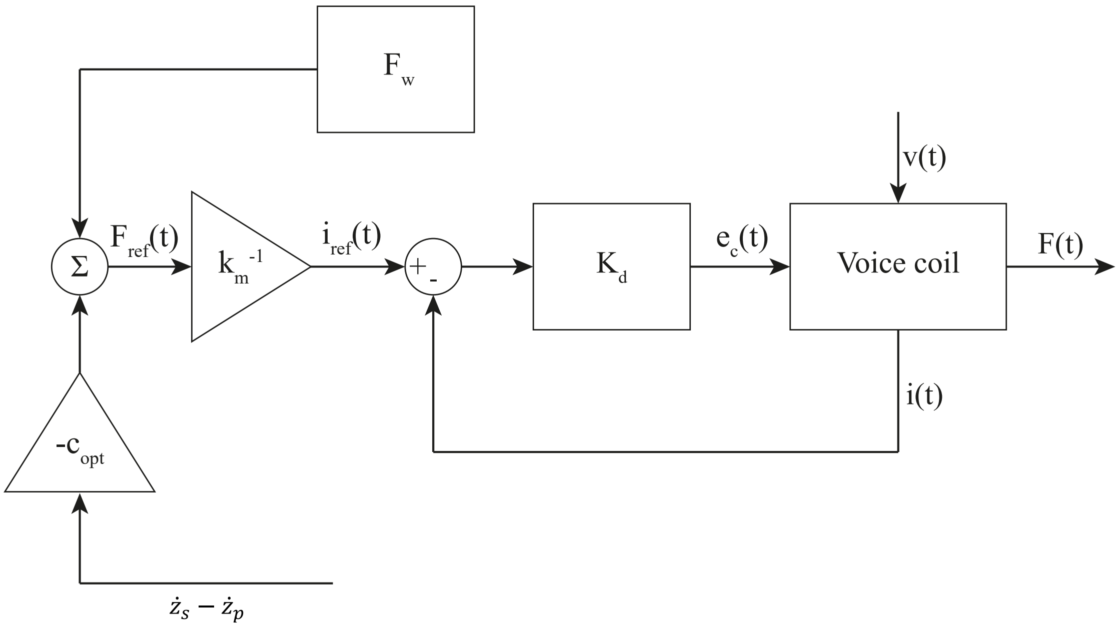

Figure 6.9: Control architecture revisited

Table 6.3 and Figures 6.10-6.12.

	P	I
1st design step	0.587	5.421
2nd design step	$4.775 \cdot 10^{-5}$	1.91

Table 6.3: PI controller parameters

The main difference between the two successive phases consists in a sharp reduction of both the proportional gain and of the integral coefficient, in order to eliminate the ringing phenomenon on the control voltage e_c. On the other hand, however, this action yields a slower force tracking transient and a more significant amplitude for the oscillations in both the unsprung mass position and sprung mass acceleration. The proposed control strategy is able, in any case, to stabilise the levitation device, as both z_p and $\ddot{z}_s$ reach a constant steady-state value.
Another advantage with respect to the static state feedback architecture is the absence of sharp peaks in the control voltage, as well as a lower steady state value that is sufficient to fulfill both control objectives. Nevertheless, this solution requires, in principle, velocity sensors, which are not featured in the original experimental procedure. However, their use can be bypassed if a velocity estimation algorithm is

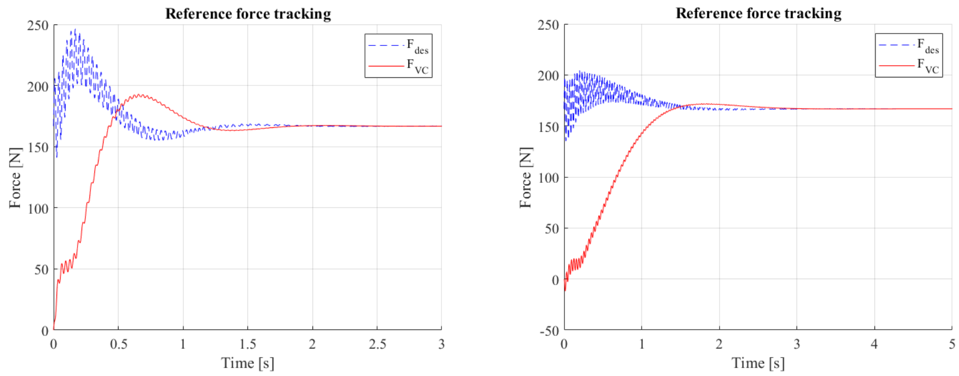

(a) 1st design step **(b)** 2nd design step

Figure 6.10: Desired force at VCA output: reference tracking

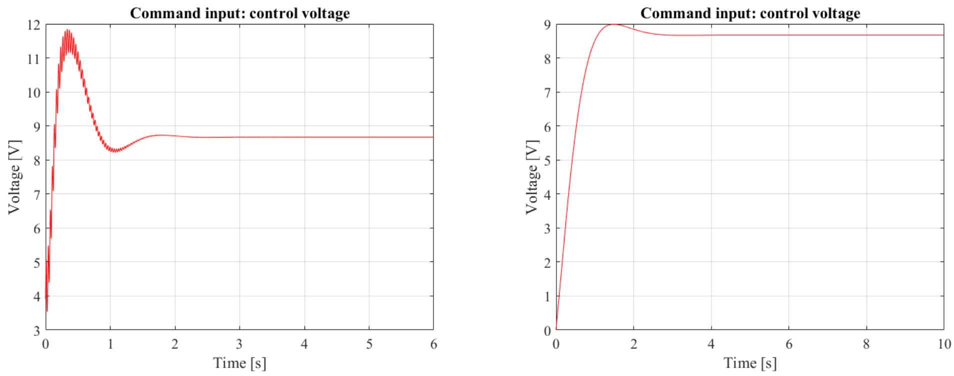

(a) 1st design step **(b)** 2nd design step

Figure 6.11: Command input: control voltage

implemented.

6.2.4 Current feedback with proportional-integral controller and velocity estimation

In order to optimise costs and simplify sensors interfaces, the damping force reference needed to realise the above described suspension control solution, shall be provided through estimation and filtering techniques. Moreover, according to the considerations on the position regulation, a new feasible architecture can be inspected in Figure 6.13.

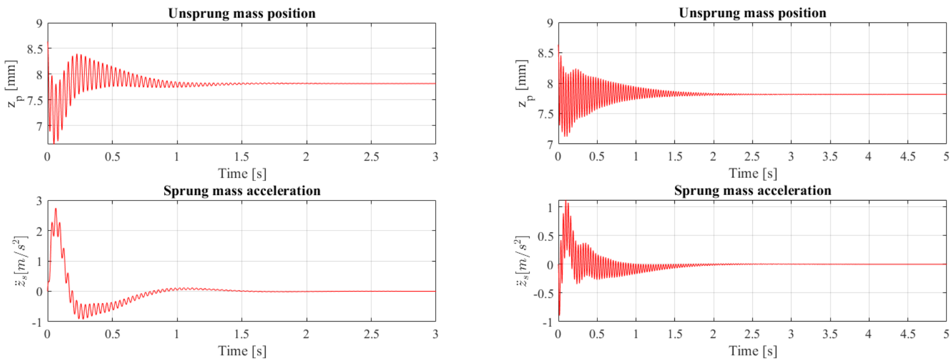

(a) 1^{st} design step **(b)** 2^{nd} design step

Figure 6.12: Output signals monitoring: unsprung mass position and sprung mass acceleration

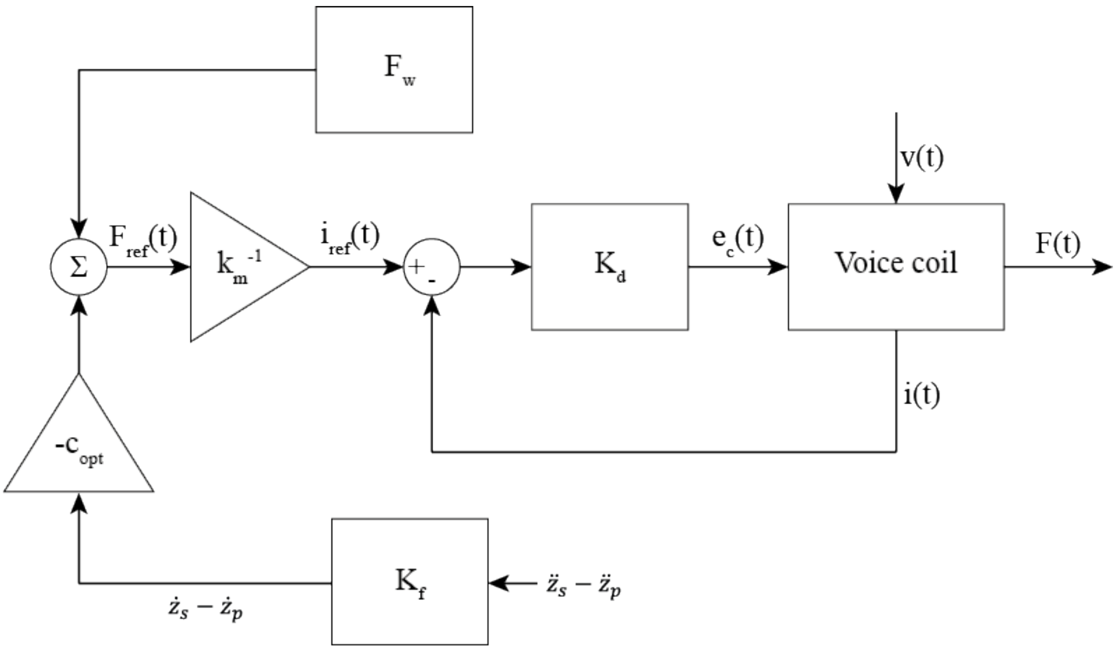

Figure 6.13: Control architecture revisited

Sensor fusion technique for velocity estimation

Classical Kalman filter theory[43] prescribes state estimation by means of input and output measurements. Therefore, the system shall be reformulated in a proper outline, that can be found in Appendix C. Nevertheless, classical estimation approaches make use of position data only; this aspect, combined with a complex mathematical description of the problem, may yield large estimation errors, which in turn may deteriorate the performances of the control system. As a consequence, the problem has been tackled by means of a different approach that is referred to as *sensor fusion*[45, 44]. In this framework, the recursive prediction and correction algorithm implemented through a Kalman filter is applied to a different system's model that enhances and correlates the information on both position and velocity. In particular, vertical dynamics is described by means of discrete time motion laws as in Equations 6.3 and 6.4.

$$z_j = z_{j-1} + T_s v_j + \frac{T_s^2}{2} a_j \tag{6.3}$$

$$v_j = v_{j-1} + T_s a_j \tag{6.4}$$

This formulation is that of a Wiener process acceleration model [46], where the index j refers to the sampling instant $t = jT_s$, $z_j = z_{s,j} - z_{p,j}$ is the relative displacement between sprung and unsprung masses; as a consequence, v_j and a_j are, respectively, the relative velocity and acceleration. It is worthwhile noticing that in this formulation, the acceleration term is constant: even though this model is an oversimplification of the behaviour of the levitation device, it is provided to the Kalman filter algorithm as an initial state estimate, that will be corrected and updated on the basis of information on output variables and noise measurements. Therefore, possible discrepancies between the model and the real system can be accounted for during successive approximations. Such model is stated in state-space representation in Equations 6.5 and 6.6, where state and output vectors and matrices are defined in Equation 6.7.

$$\mathbf{x}_j = \mathbf{\Phi}\mathbf{x}_{j-1} + \mathbf{w}_{j-1} \tag{6.5}$$

$$\mathbf{y}_j = \mathbf{H}\mathbf{x}_j + \mathbf{v}_j \tag{6.6}$$

$$\mathbf{x}_j = [z_j \; v_j \; a_j]^T \quad \mathbf{\Phi} = \begin{bmatrix} 1 & T_s & T_s^2/2 \\ 0 & 1 & T_s \\ 0 & 0 & 1 \end{bmatrix} \qquad \mathbf{y}_j = [z_j \; a_j]^T \quad \mathbf{H} = \begin{bmatrix} 1 & 0 & 0 \\ 0 & 0 & 1 \end{bmatrix} \tag{6.7}$$

The input and output noise vectors $\mathbf{w}_j$ and $\mathbf{v}_j$ account for, respectively, modelling inaccuracies and measurements noise, and they are defined by covariance matrices $\mathbf{Q}$ and $\mathbf{R}$ respectively. In particular, the matrix $\mathbf{Q}$ depends on the process covariance σ_q^2, and its structure is defined in Equation 6.8 according to the Wiener process acceleration model.

$$\mathbf{Q} = \sigma_q^2 \begin{bmatrix} \frac{1}{20}T_s^5 & \frac{1}{8}T_s^4 & \frac{1}{6}T_s^3 \\ \frac{1}{8}T_s^4 & \frac{1}{3}T_s^3 & \frac{1}{2}T_s^2 \\ \frac{1}{6}T_s^3 & \frac{1}{2}T_s^2 & T_s \end{bmatrix} \tag{6.8}$$

The output covariance matrix defined in Equation 6.9 accounts for the sensors' uncertainty ranges through their variances. In this framework, measured data are considered uncorrelated.

$$\mathbf{R} = \begin{bmatrix} \sigma_{r,z}^2 & 0 \\ 0 & \sigma_{r,a}^2 \end{bmatrix} \tag{6.9}$$

In the forthcoming assessments, given the lack of information on the sensors to be employed, the output variances will be set to $\sigma_{r,z}^2 = \sigma_{r,a}^2 = 0.1$. The process covariance has instead been set by trial and error, by simulating the model described by equations in Appendix C. A suitable value that minimises the velocity estimation error (Figure 6.14) is:

$$\sigma_q^2 = 0.01 \tag{6.10}$$

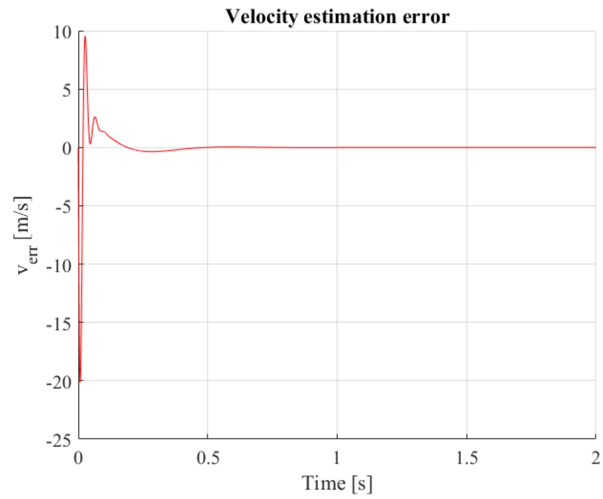

Figure 6.14: Velocity estimation error

Controller design and simulation outcomes

Given the above described Kalman filter, that feeds the control algorithm with a velocity and, therefore, a damping force reference, the proportional and integral coefficient have been tuned, in two successive steps, to achieve stability of the closed loop system and acceptable tracking accuracy. Parameters are reported in Table 6.4, while the evolution of the output versus desired force, actuation voltage and output position and acceleration are reported in Figures 6.15 to 6.17.
The first proposed solution shows interesting properties in terms of transient tracking, and it does not yield significant oscillations neither in the control voltage e_c nor in the evolution of the sprung mass position z_p and sprung mass acceleration

	P	I
1^{st} design step	21.964	1707.244
2^{nd} design step	5.964	407.244

Table 6.4: PI controller parameters

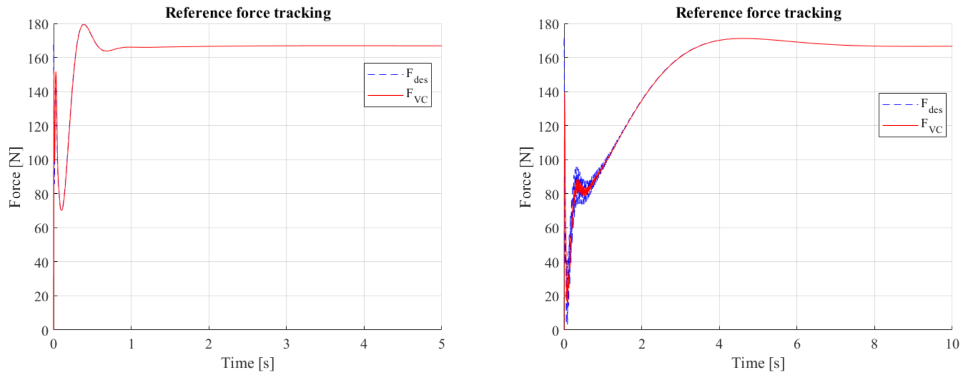

(a) 1^{st} design step **(b)** 2^{nd} design step

Figure 6.15: Desired force at VCA output: reference tracking

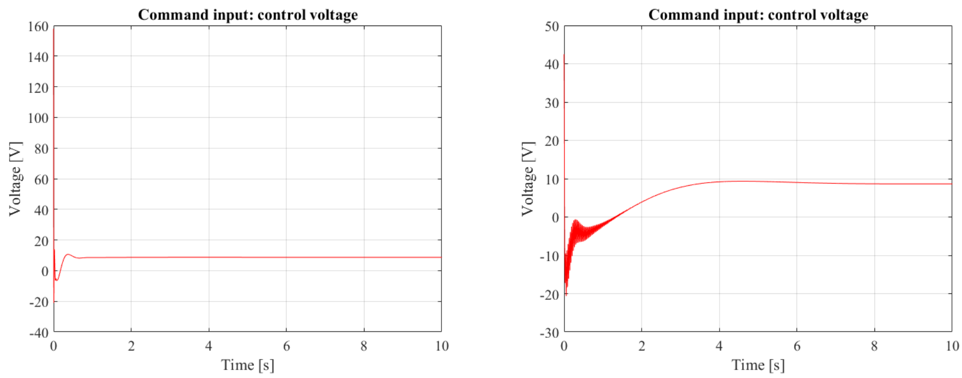

(a) 1^{st} design step **(b)** 2^{nd} design step

Figure 6.16: Command input: control voltage

$\ddot{z}_s$. However, the peak value in the control voltage is here equal to $e_{c,max} \approx 157$V, while the maximum voltage for the DC bus used to power the VCA is equal to 48V. Hence the necessity for a further design step aimed at reducing the command effort. What has been proposed succeeds in this objective, but higher oscillations and ripple phenomena are introduced.
As a conclusion, despite being extremely interesting from a scientific viewpoint, this architecture requires further analysis on the structure of the controller: a *model*

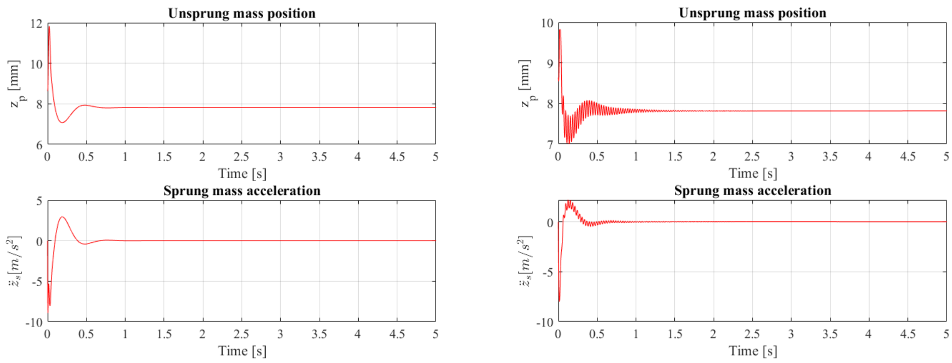

(a) 1st design step **(b)** 2nd design step

Figure 6.17: Output signals monitoring: unsprung mass position and sprung mass acceleration

predictive control based solution[47], that allows to account for input saturation explicitly, could be able to attain minimal control effort along with optimal tracking performances.

6.3 Code generation and platform deployment

Given the proposed control algorithms solutions, the successive step to assess their behaviour consists in transforming the Simulink®into hardware-readable code. To this end, the automatic code generation provided by the modelling software is employed. The target board is a Texas Instruments®LaunchPad™ (datasheet in Ref.[48]). The hardware comes with digital and analogue GPIO pins, four independent 16-bits ADC converters and a C28x CPU, which is a 32-bits fixed point processor. The board is interfaced with a BOOSTXL™ driver (datasheet in Ref.[49]), which is a six-step inverter, supplied with a DC power supply equal to 18V, whose purpose consists in driving the VCA with the required control voltage e_c. As represented in Figure 6.18, an inverter provides its load with current, whose waveform depends on the behaviour of the switches: the designer can control the duty cycle of their driving signal, to determine the extent to which the constant voltage coming from the DC bus goes through the leg of the inverter and, therefore, to the load.
To this end, it is necessary to adjust the proposed control algorithms to transform the command input e_c in the input duty cycle D_c for the actuator's driver. This issue is dealt with in the following section, along with a detailed description of the interface between the actual controller, board sensors and the host PC. Afterwards, the processor-in-the-loop test framework is introduced, along with algorithm test

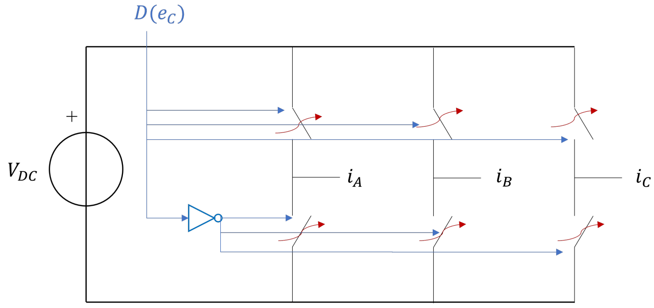

Figure 6.18: Six-step inverter, electrical scheme

results.

6.3.1 Algorithm structure

The proposed workflow exploits two different Simulink models. The **host**, allows selection of the reference damping and system enabling, while establishing the serial communication between the PC and the board: it transmits the above mentioned signals via interrupt mechanism and it retrieves and displays the current at the output of the inverter, measured through a probe on the device, as well as the input duty cycle. Its block diagram representation is found in Figure 6.19. Such model runs on a PC, and automatically triggers the board.

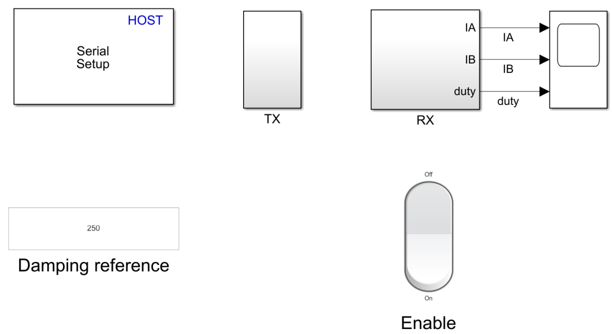

Figure 6.19: Host block diagram

The target hardware instead features the code corresponding to the model in Figure 6.20.

- At first, the signals coming from the host, along with the detected interrupt, are processed through hardware-specific blocks on its serial interface. Afterwards, they are decoupled and transmitted to the actual control algorithm;
- The controller is composed by three subsystems:

- the "Inverter driving" module takes the duty cycle proportional to the control voltage e_c as input, and it uses it to drive the switches that control the inverter. Moreover, it features the ADC interface that measures the current at the output of the inverter;
- the "mechanical domain" block models the experimental procedure in mathematical terms, as already discussed in previous sections (see Figure 6.1). At this stage, such modelling is necessary to assess the real-time behaviour of the control system, since the remaining part of the bench is still not available. Moreover, the VCA does not work without a mechanical load: therefore, the inverter drives a coil with current, and thus the mechanical port of the voice coil is also included in this model.
- the true controller algorithm is implemented in the self-titled subsystem, which takes the reference damping, the measured current and the relative velocity between sprung and unsprung masses as input, and it provides at its output the duty cycle D_c proportional to the control voltage

Rate transition blocks allow the mechanical domain model to be simulated with a slower pace with respect to the remainder of the code, in order not to overload the board too much. This code is deployed on the board by means of the Simulink® package *Embedded Coder*.

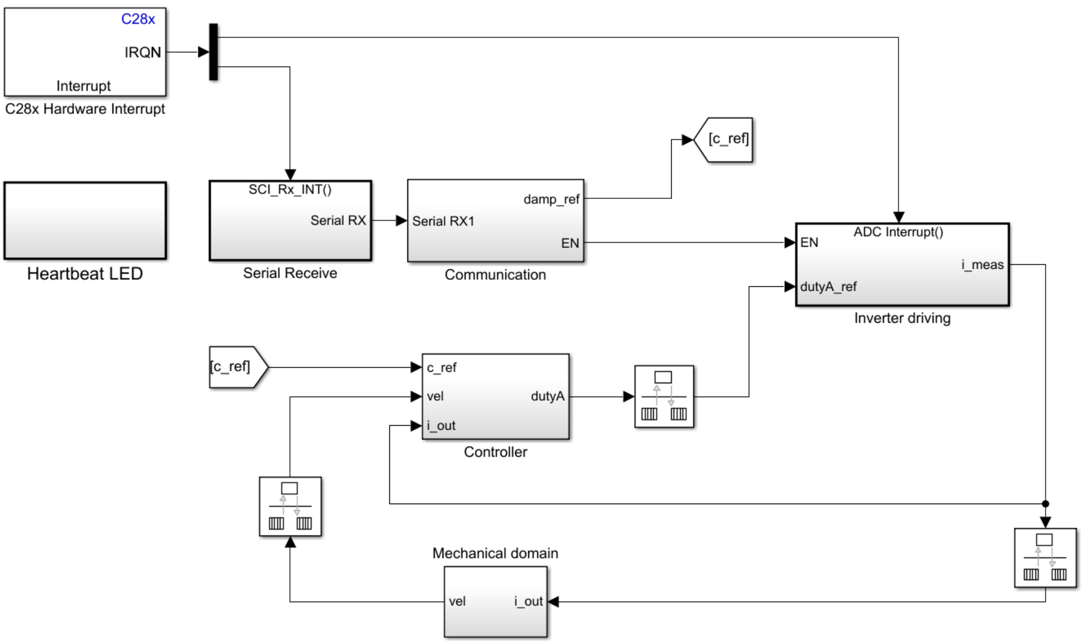

Figure 6.20: Target hardware model block diagram

6.3.2 Processor-in-the-loop framework

In the model-based design scenario an important step is represented by processor-in-the-loop tests. In this framework, the control algorithm runs on the target board, while the physical system's description is a mathematical model simulated on the host PC. In principle, the test architecture would be the one represented in Figure 6.21.

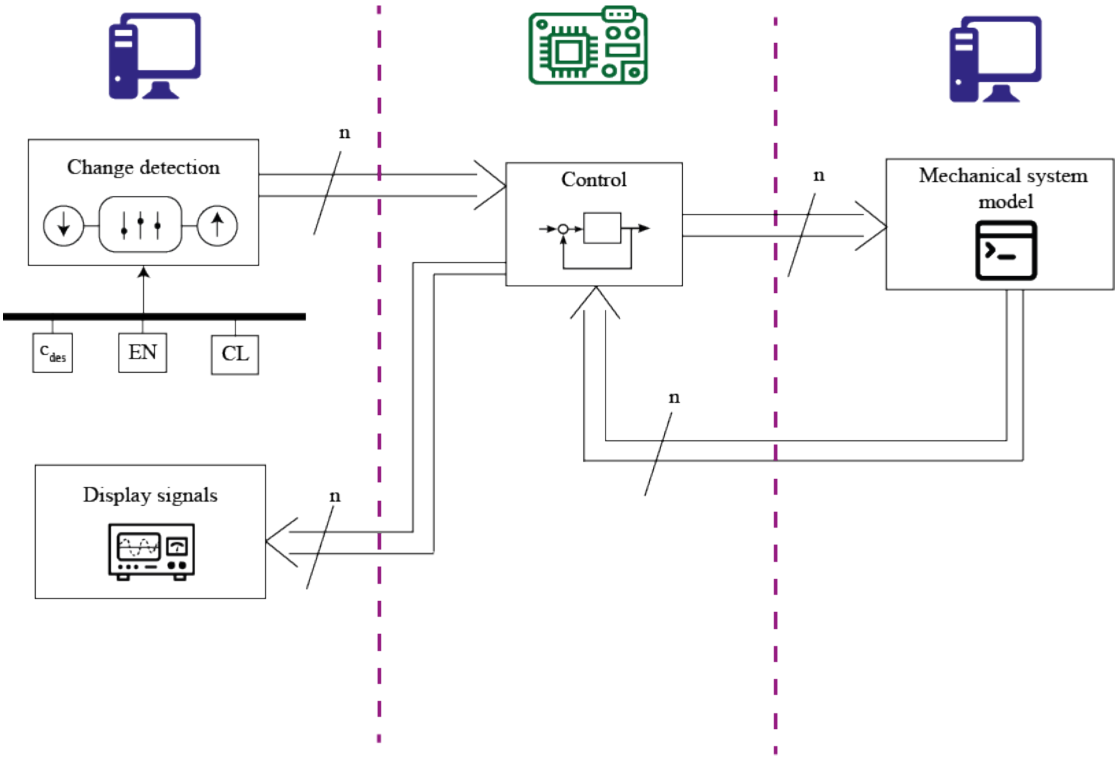

Figure 6.21: PIL test architecture

However, the actuator (i.e. the inverter) does not provide any output current if unloaded. Therefore, the control loop cannot be closed. Information coming from a test harness of the proposed control algorithm would not provide useful insight to the validation procedure, since the overall framework would be very similar to the already discussed model-in-the-loop one: the controller should still run on the host PC, therefore its real time capabilities cannot be investigated.

6.4 Hardware-in-the-loop framework

A further step in the assessment of the suspension control strategies is the hardware-in-the-loop framework: here, the controller is deployed on the target hardware, and it is connected to the physical system, or to a machine that emulates its real time capabilities and interconnections.

6.4.1 Test layout

However, in this case the physical system was not yet available in its entirety. Therefore, an alternative solution is here employed, and its qualitative flow is featured in Figure 6.22.

1. The host PC provides to the target hardware the reference damping and enabling signal.
2. The control algorithm runs on the board, and it drives the inverter with the duty cycle D_c, proportional to the desired control voltage e_c.
3. The six step inverter produces the current i_{out} that drives the coil.
4. Such current is sensed through probes and sent back to the hardware by means of the ADC converter: its value closes the control loop, and is fed to the mechanical domain subsystem, that also runs on the target platform to ensure real-time operation during the whole experiment.

6.4.2 Results

Coil identification

In order to adapt the control algorithm to the new test scenario, the equivalent lumped resistance R_c and inductance L_c of the coil shall be estimated. To this end, the coil has been provided with a voltage step, and the current through it has been measured. The I-V relation has been modelled through the well-known equation for a RL circuit (Equation 6.11), so that experimentally retrieved data are fit to the model by means of the least squares algorithm.

$$I(t) = \frac{V_0(t)}{R_c}\left(1 - e^{-R_c/L_c \cdot t}\right) \tag{6.11}$$

Values for the required parameters along with their 95% confidence interval are stated in Table 6.5. The root mean square error on the current is equal to $RMSE = 8\text{mA}$. The employed experimental data have been generated through the same target MCU needed to implement the suspension control algorithms: a DC bus with $V_{DC} = 20.75\text{V}$ was used as a supply for the inverter, that has been provided with $D_c = 5\%$, thus yielding $V_0 = D_c \cdot V_{DC} = 1.033\text{V}$. Therefore, the current through the coil has been measured and served as input in the fitting

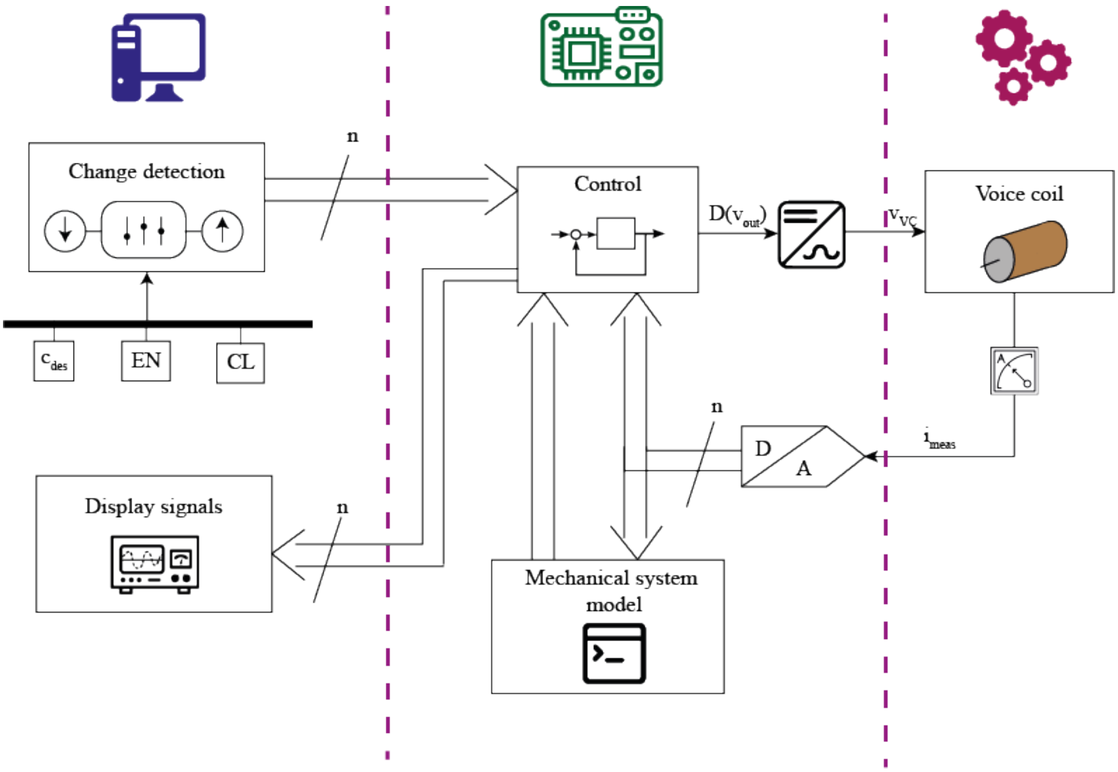

Figure 6.22: HIL test architecture

	X_{min}	X_c	X_{max}
R, $[\Omega]$	0.7977	0.7982	0.7988
L, [mH]	0.5169	0.5205	0.524

Table 6.5: RL description for the coil: identified parameters

procedure. The outcome of such process in terms of measured data versus identified model can be inspected in Figure 6.23.

Test outcomes

In the described framework, the admissible voltages, currents and power levels are much lower than those that will be featured in the actual test bench. In particular, with a DC bus that delivers approximately 20V, and considering the equivalent resistance of the coil to be used as a load, it is safe to limit the steady state current flow to $i_{max} = 2$A. This sets an upper bound on the constant output voltage equal to 1.6V.
These limitations, however, are not compliant with the control effort time evolution

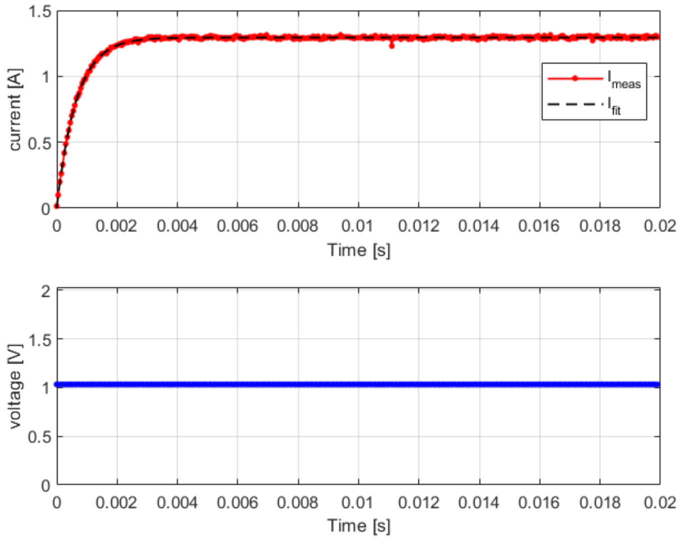

Figure 6.23: RL circuit identification:experimental data vs. model output

reported in Figure 6.7, which requires a maximum voltage equal to 17V approximately, and a steady state value of V. Therefore, a possible solution consists in down-scaling the masses of the capsule and of the bogie, in order to obtain acceptable signal values. In particular, if one sets the unsprung and sprung masses as in Equation 6.12, the new control law coefficient and system response in terms of reference tracking, command input and output variables are summarised in Equation 6.13 and Figures 6.24 and 6.25 respectively.

$$m_u = 0.1\text{kg} \qquad m_s = 1\text{kg} \tag{6.12}$$

$$\alpha = 1.7303\Omega \qquad e_w = 0.981\text{V} \tag{6.13}$$

Simulation outcomes in terms of control voltage and current through the coil are reported in Figure 6.26. The time evolution of the above mentioned signals present a piecewise behaviour.

- When the "ENABLE" signal is low, the control algorithm is inactive, since the switches that regulate the current at the output of the inverter are open (this operation is achieved through a logic "AND"); in this scenario, the current probe measures its full-scale by default. Due to this acquisition, given the control law in Equation 6.14, the control voltage should take the value $V_{EN=0} = 21.06$V: however, such signal has been allowed to vary in the range

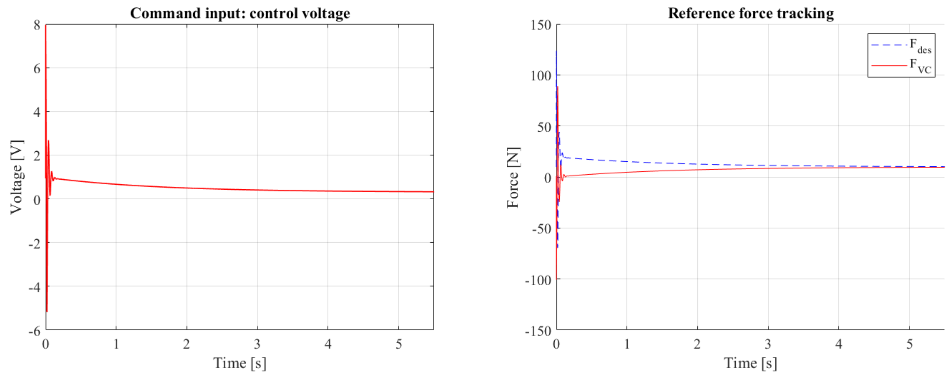

(a) Control effort **(b)** Reference force tracking

Figure 6.24: Controller performances.

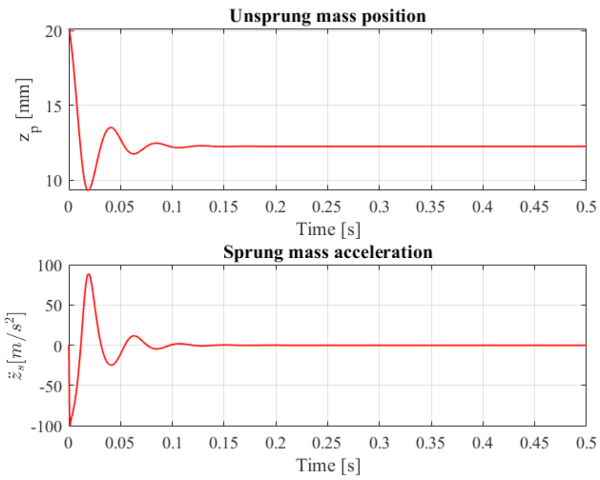

Figure 6.25: Output variables

$[0 \div 5]$V, for the above defined limitation on the current through the coil.

$$e_c = -\alpha i_{meas} + \frac{m_s g}{km}(R + \alpha) \tag{6.14}$$

- when the algorithm has been enabled, the system follows the prescribed control law, apart from a short time interval in which the voltage saturates to 0V.

When compared to numerical simulation results, the deployed controller reaches the same (and expected) steady-state voltage value $e_{ss} = 0.311$V, but with a much faster transient and fewer oscillations. This may be due to the lack of an actual mechanical interface in the test scenario: the coil affects the behaviour of

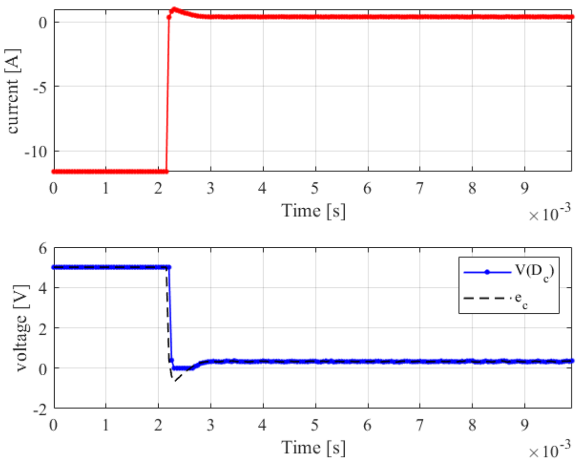

Figure 6.26: Functional test outcome

the simulated quarter-car model, but the vice-versa cannot happen. A possible solution consists in building a ficticious mechanical port through the force constant K_m that characterises the voice coil (see Section 5.1.1): the additional voltage term $e_{VC} = -K_m \left(\dot{z}_s - \dot{z}_p\right)$ can be added to the control input e_c that drives the coil through the inverter. However, this strategy has proven ineffective, since the additional voltage brings the overall output signal to saturation, as it can be inspected from the time evolution of the signal in Figure 6.27.

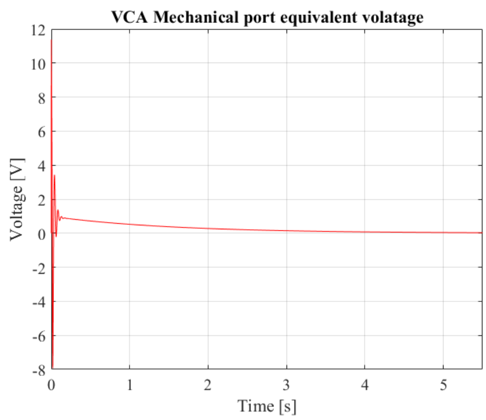

Figure 6.27: Equivalent voltage of the mechanical port of the voice coil actuator

Nevertheless, the deployment of the control algorithm *per se* on the target platform yielded satisfactory results: the additional mechanical term explains the transient discrepacy between the simulation and test control voltage outcome, and it can be solved in a straightforward way during actual test bench assessments: in this scenario, a DC power supply with higher V_{max} will be employed. Moreover, the additional signal is internal to the actuator, and does not impose alterations to the proposed control algorithm.

Chapter 7

Conclusions and further studies

The rising awareness on climate change, combined with the increasing possibility to travel has conveyed, over the last few decades, the efforts of both the research community and governing agencies towards the quest for a fast, reliable and sustainable mean of transportation. Among the possible proposed solutions, the framework of magnetic levitation trains is particularly attractive, due to its virtually zero-emission propulsion, and reching of very high speeds, up to 600km/h. A substantial improvement in this direction comes from the Hyperloop technology: it still features magnetic levitation, but capsules are enclosed in evacuated tubes. This yields minimally influent air friction phenomena, and in turn ultra high cruise speed (up to 1200km/h).
Recent research work address the modelling and implementation of the infrastucture and propulsion mechanisms, as well as the aerodynamic behaviour of the whole system. However, the levitation subsystem, which can be considered the enabling technology of a Hyperloop-based transportation, remains partially unexplored. The goal is to implement capsule suspension through passive electrodynamic technologies; however, such a solution introduces an intrinsically unstable behaviour, that has been rigorously assessed by Galluzzi et al. In particular, the authors provide a multi-domain modelling approach that combines accurate eddy current distribution description within the electromagnetic domain and coupling with the mechanical variables that describe levitation in its vertical dynamics. Such technique is able to capture and compensate with additional damping, the instability of the system, that occurs indeed when the two domains are connected. Moreover, this model has been validated by Circosta et al. on a multi-degrees-of-freedom representation of the capsule.

This thesis outlines the main steps of the design procedure for an experimental

test rig, whose purpose is the assessment of the above described model for a Hyperloop-like levitation system, as well as of the proposed stabilisation techniques. After a synthetic literature review, the structure of the test bench has been discussed and motivated, and relevant physical variables have been described. Afterwards, modelling of a laboratory-sized prototype has been carried out, motivating the final choice in terms of scale factor. After having assessed the unstable behaviour of the system, and having introduced the additional damping value that optimises natural modes convergence, suspension design and control methodologies have been addressed.
Three control architecture are introduced, implemented and compared in terms of both performances and complexity. Finally, functional tests on the target MCU platform have been described, along with relevant experimental results.

Despite the tested control strategy shows acceptable performances in terms of steady-state tracking error and maximum control effort, being able to implement an optimal solution that features sensor fusion and velocity estimation by means of a Kalman filter would be beneficial, since it allows more flexibility in the design of the control strategy. A MPC based architecture could be able to combine input saturation limits with optimal performances. Nevertheless, a target hardware platform with the necessary computing power shall be available.

Appendix A

2-DOF state matrix for the dynamic levitation system

$$\mathbf{x} = \{i_{d,1} \quad i_{q,1} \quad \dots \quad i_{d,N_b} \quad i_{q,N_b} \quad \dot{z}_p \quad z_p \quad \dot{z}_s \quad z_s\}^T \tag{A.1}$$

$$A = \begin{bmatrix} \mathbf{A_{el}} & \mathbf{A_{ep}} \\ \mathbf{A_{pe}} & \mathbf{A_{m}} \end{bmatrix} \tag{A.2}$$

$$\mathbf{A_{el}} = \begin{bmatrix} -\omega_{p,1} & \omega & 0 & \dots & 0 & 0 \\ -\omega & -\omega_{p,1} & 0 & \dots & 0 & 0 \\ \vdots & \vdots & \vdots & \ddots & \vdots & \vdots \\ 0 & 0 & 0 & \dots & -\omega_{p,N_b} & \omega \\ 0 & 0 & 0 & \dots & -\omega & -\omega_{p,N_b} \end{bmatrix} \tag{A.3}$$

$$\begin{aligned} \mathbf{A_{ep}} &= \begin{bmatrix} \frac{\Lambda_0}{\gamma L_1} e^{-z_{p,0}/\gamma} & 0 & 0 & 0 \\ 0 & \frac{\Lambda_0}{\gamma L_1} e^{-z_{p,0}/\gamma} & 0 & 0 \\ \vdots & \vdots & \vdots & \vdots \\ \frac{\Lambda_0}{\gamma L_{Nb}} e^{-z_{p,0}/\gamma} & 0 & 0 & 0 \\ 0 & \frac{\Lambda_0}{\gamma L_{Nb}} e^{-z_{p,0}/\gamma} & 0 & 0 \end{bmatrix} \\ \mathbf{A_{pe}} &= \begin{bmatrix} -\frac{2\Lambda_0}{\gamma m_p} e^{-z_{p,0}/\gamma} & 0 & \dots & -\frac{2\Lambda_0}{\gamma m_p} e^{-z_{p,0}/\gamma} & 0 \\ 0 & 0 & \dots & 0 & 0 \\ 0 & 0 & \dots & 0 & 0 \\ 0 & 0 & \dots & 0 & 0 \end{bmatrix} \end{aligned} \tag{A.4}$$

$$\mathbf{A_m} = \begin{bmatrix} -\frac{c_s}{m_p} & -\frac{k_s+k_{us}}{mp} & \frac{c_s}{m_p} & \frac{k_s}{m_p} \\ 1 & 0 & 0 & 0 \\ \frac{c_s}{m_s} & -\frac{k_s}{ms} & -\frac{c_s}{m_s} & -\frac{k_s}{m_s} \\ 0 & 0 & 1 & 0 \end{bmatrix} \tag{A.5}$$

Appendix B

Bearing loads evaluation: free body diagrams

Figure B.1: Disk free body diagram

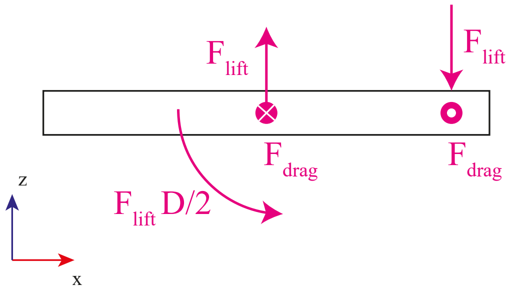

(a) Disk, xz plane

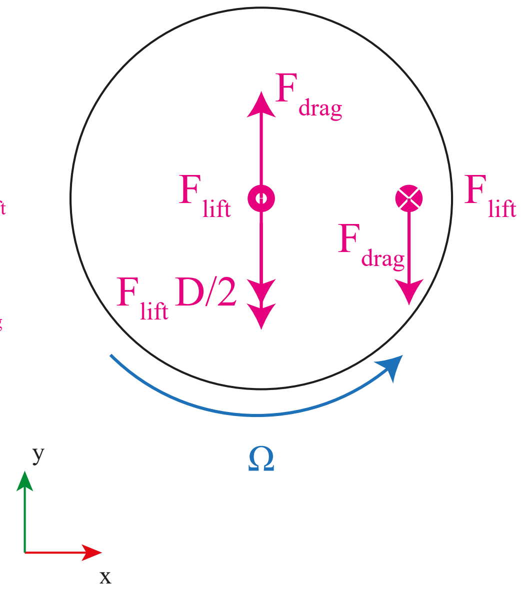

(b) Disk, xy plane

Figure B.2: Shaft free body diagrams

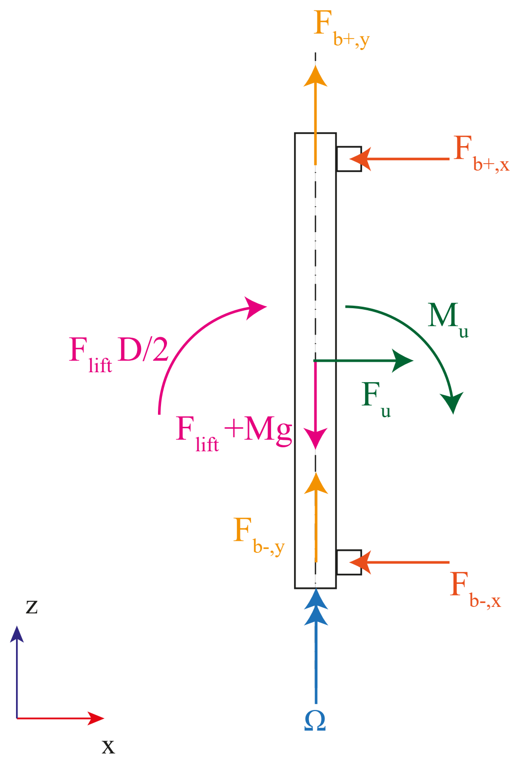

(a) Shaft and bearings, xz plane

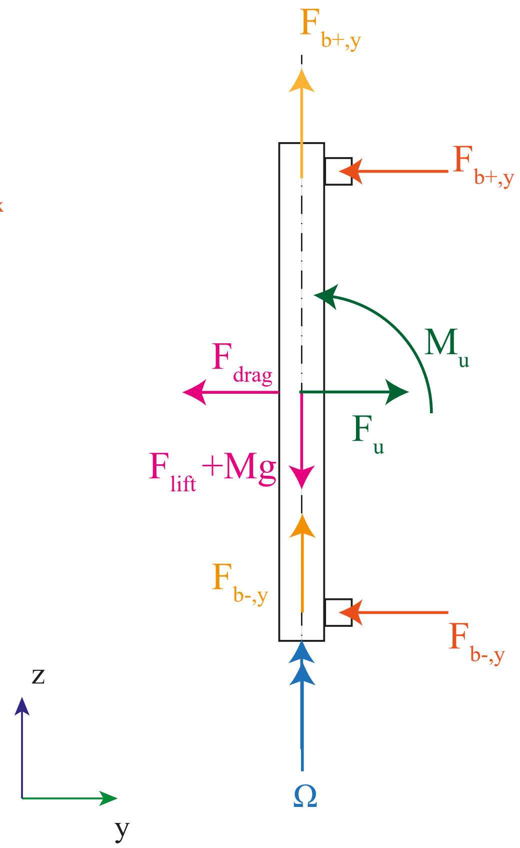

(b) Shaft and bearings, yz plane

Appendix C

2-DOF linear-time-invariant system for velocity estimation

$$\dot{\mathbf{x}}_e = \mathbf{A}_e\mathbf{x}_e + \mathbf{B}\mathbf{u}_e \tag{C.1}$$

$$\mathbf{y}_e = \mathbf{C}_e\mathbf{x}_e + \mathbf{D}\mathbf{u}_e \tag{C.2}$$

$$\mathbf{x}_e = \begin{bmatrix}\mathbf{x} & z_{in}\end{bmatrix} \tag{C.3}$$

$$\mathbf{A}_e = \begin{bmatrix}\mathbf{A} & \mathbf{a}\\ \mathbf{0} & 0\end{bmatrix} \tag{C.4}$$

$$\mathbf{a} = \begin{bmatrix}0 & -\frac{\omega\Lambda_0}{\gamma L_1}e^{-z_{p,0}/\gamma} & \dots & 0 & -\frac{\omega\Lambda_0}{\gamma L_{N_b}}e^{-z_{p,0}/\gamma} & 0 & 0 & 0 & 0\end{bmatrix} \tag{C.5}$$

$$\mathbf{u} = \dot{z}_{in} = v_{in} \tag{C.6}$$

$$\mathbf{B} = \begin{bmatrix}-\frac{\Lambda_0}{\gamma L_1}e^{-z_{p,0}/\gamma} & 0 & \dots & -\frac{\Lambda_0}{\gamma L_{N_b}}e^{-z_{p,0}/\gamma} & 0 & 0 & 0 & 0 & 0 & 1\end{bmatrix}^T \tag{C.7}$$

$$\mathbf{y} = \begin{bmatrix}z_p & z_s\end{bmatrix} \tag{C.8}$$

$$C = \begin{bmatrix}0 & \dots & 0 & 1 & 0 & 0\\ 0 & \dots & 0 & 0 & 0 & 1\end{bmatrix} \tag{C.9}$$

$$D = \begin{bmatrix}0 & 0\end{bmatrix}^T \tag{C.10}$$

Bibliography

[1] Michael E. Webber. «Electric Highway». In: *Mechanical Engineering* 141.06 (June 2019), pp. 32–37. ISSN: 0025-6501 (cit. on p. 1).

[2] Mitchell van Balen et al. «EU transport research innovation status assessment report - An overview based on the Transport Research and Innovation Monitoring and Information System (TRIMIS) database». In: Aug. 2019. DOI: 10.2760/6954 (cit. on p. 1).

[3] Han H. and Kim D. *Magnetic Levitation. Maglev Technology and Applications.* 2016 (cit. on p. 1).

[4] 2013 SpaceX. *Hyperloop Alpha.* URL: https://www.tesla.com/sites/default/files/blog_images/hyperloop-alpha.pdf (cit. on pp. 2, 49).

[5] R.F. Post and D.D. Ryutov. «The Inductrack: a simpler approach to magnetic levitation». In: *IEEE Transactions on Applied Superconductivity* 10.1 (2000), pp. 901–904. DOI: 10.1109/77.828377 (cit. on pp. 2, 4).

[6] Gurol H. et al. *General Atomics Low Speed Maglev Technology Development Program (Supplemental 3).* Tech. rep. United States. Federal Transit Administration. Office of Technology, 2005 (cit. on p. 3).

[7] MMJ Opgenoord et al. «MIT hyperloop final report». In: *Massachusetts Institute of Technology, Cambridge, Massachusetts* (2017) (cit. on pp. 3, 4).

[8] Renato Galluzzi et al. «A Multi-domain Approach to the Stabilization of Electrodynamic Levitation Systems». In: *Journal of Vibration and Acoustics* 142.6 (2020) (cit. on pp. 4, 5, 12, 13, 39).

[9] Nicholas A. Alexander and Mohammad M. Kashani. «Exploring Bridge Dynamics for Ultra-high-speed, Hyperloop, Trains». In: *Structures* 14 (2018), pp. 69–74. ISSN: 2352-0124. DOI: https://doi.org/10.1016/j.istruc.2018.02.006. URL: https://www.sciencedirect.com/science/article/pii/S2352012418300249 (cit. on p. 4).

[10] N. Nick and Yohei Sato. «Computational fluid dynamics simulation of Hyperloop pod predicting laminar–turbulent transition». In: *Railway Engineering Science* 28 (2020), pp. 97–111 (cit. on p. 4).

[11] Su Y. Choi et al. «Sub-Sonic Linear Synchronous Motors Using Superconducting Magnets for the Hyperloop». In: *Energies* 12.24 (2019). ISSN: 1996-1073. DOI: 10.3390/en12244611. URL: https://www.mdpi.com/1996-1073/12/24/4611 (cit. on p. 4).

[12] Fabrizio Impinna et al. «Passive Magnetic Levitation of Rotors on Axial Electrodynamic Bearings». In: *IEEE Transactions on Magnetics* 49.1 (2013), pp. 599–608. DOI: 10.1109/TMAG.2012.2209124 (cit. on p. 4).

[13] Eric Chaidez, Shankar P. Bhattacharyya, and Adonios N. Karpetis. «Levitation Methods for Use in the Hyperloop High-Speed Transportation System». In: *Energies* 12.21 (2019). ISSN: 1996-1073. DOI: 10.3390/en12214190. URL: https://www.mdpi.com/1996-1073/12/21/4190 (cit. on p. 4).

[14] Andrea Tonoli. «Dynamic characteristics of eddy current dampers and couplers». In: *Journal of Sound and Vibration* 301.3 (2007), pp. 576–591. ISSN: 0022-460X. DOI: https://doi.org/10.1016/j.jsv.2006.10.015. URL: https://www.sciencedirect.com/science/article/pii/S0022460X0600798X (cit. on p. 4).

[15] J.G. Detoni et al. «Unified modelling of passive homopolar and heteropolar electrodynamic bearings». In: *Journal of Sound and Vibration* 331.19 (2012), pp. 4219–4232. ISSN: 0022-460X. DOI: https://doi.org/10.1016/j.jsv.2012.04.036. URL: https://www.sciencedirect.com/science/article/pii/S0022460X12003550 (cit. on p. 4).

[16] A.V. Filatov and E.H. Maslen. «Passive magnetic bearing for flywheel energy storage systems». In: *IEEE Transactions on Magnetics* 37.6 (2001), pp. 3913–3924. DOI: 10.1109/20.966127 (cit. on p. 4).

[17] Torbjörn A Lembke. «Design and analysis of a novel low loss homopolar electrodynamic bearing». PhD thesis. KTH, 2005 (cit. on p. 4).

[18] TA Lembke. «Review of electrodynamic bearings». In: *14th International Symposium on Magnetic Bearings (ISMB)*. 2014, pp. 257–262 (cit. on p. 4).

[19] Richard F Post. *Inductrack demonstration model*. Tech. rep. Lawrence Livermore National Lab., CA (United States), 1998 (cit. on p. 4).

[20] M. M. Khan. *Development of Ryerson's First Hyperloop Pod for Systems Using a Modular Approach*. 2019 (cit. on p. 4).

[21] J Íñiguez and V Raposo. «Laboratory scale prototype of a low-speed electrodynamic levitation system based on a Halbach magnet array». In: *European journal of physics* 30.2 (2009), p. 367 (cit. on p. 4).

[22] Zhaoyu Guo, Jie Li, and Danfeng Zhou. «Study of a null-flux coil electrodynamic suspension structure for evacuated tube transportation». In: *Symmetry* 11.10 (2019), p. 1239 (cit. on p. 4).

[23] Jiaheng Duan et al. «Analysis and optimization of asymmetrical double-sided electrodynamic suspension devices». In: *IEEE Transactions on Magnetics* 55.6 (2019), pp. 1–5 (cit. on p. 4).

[24] Yin Chen et al. «A 3-D analytic-based model of a null-flux Halbach array electrodynamic suspension device». In: *IEEE Transactions on Magnetics* 51.11 (2015), pp. 1–5 (cit. on p. 4).

[25] Ruiyang Wang and Bingen Yang. «A Transient Model of Inductrack Dynamic Systems». In: *International Design Engineering Technical Conferences and Computers and Information in Engineering Conference*. Vol. 59285. American Society of Mechanical Engineers. 2019, V008T10A062 (cit. on p. 4).

[26] Ruiyang Wang and Bingen Yang. «Transient Response of Inductrack Systems for Maglev Transport: Part II—Solution and Dynamic Analysis». In: *Journal of Vibration and Acoustics* 142.3 (2020) (cit. on p. 4).

[27] Salvatore Circosta et al. «Passive Multi-Degree-of-Freedom Stabilization of Ultra-High-Speed Maglev Vehicles». In: *Journal of Vibration and Acoustics* 143.6 (2021), p. 061003 (cit. on p. 4).

[28] *AKMServo Motor selection guide*. Kollmorgen. URL: `https://www.kollmorgen.com/sites/default/files/Kollmorgen_AKM_Servomotor_Selection_Guide.pdf` (cit. on p. 14).

[29] ISO Central Secretary. *Mechanical vibration and shock — Evaluation of human exposure to whole-body vibration — Part 1: General requirements*. Standard ISO 2631-1:1997. Geneva, CH: International Organization for Standardization, 1997. URL: `https://www.iso.org/standard/7612.html` (cit. on p. 18).

[30] 2016 SpaceX. *SpaceX Hyperloop Test-Track Specification*. URL: `https://cdn.atraining.ru/docs/TubeSpecs.pdf` (cit. on p. 23).

[31] Robert C. Weast. *Handbook of Chemistry and Physic, 64th ed.* CRC Press, 1984. ISBN: 9780849304644 (cit. on p. 23).

[32] Douglas C. Giancoli. *Physic, 4th ed.* Prentice Hall, 1995. ISBN: 9780131834682 (cit. on p. 23).

[33] Roshan Pradhan and Aditya Katyayan. «Vehicle dynamics of permanent-magnet levitation based Hyperloop capsules». In: *Dynamic Systems and Control Conference*. Vol. 51906. American Society of Mechanical Engineers. 2018, V002T22A004 (cit. on p. 28).

[34] Hitoshi Tsunashima and Masato Abe. «Static and dynamic performance of permanent magnet suspension for maglev transport vehicle». In: *Vehicle System Dynamics* 29.2 (1998), pp. 83–111 (cit. on p. 28).

[35] Giancarlo Genta. *Vibration Dynamics and Control*. Mechanical Engineering Series. Springer, 2009. ISBN: 9780198520115 (cit. on pp. 32, 40).

[36] ISO Central Secretary. *Mechanical vibration — Rotor balancing — Part 11: Procedures and tolerances for rotors with rigid behaviour*. Standard ISO 21940-11:2016. Geneva, CH: International Organization for Standardization, 2016. URL: https://www.iso.org/obp/ui/#iso:std:iso:21940:-11:ed-1:v1:en (cit. on p. 33).

[37] *SKF bearings and mounted products*. SKF group. Apr. 2018 (cit. on p. 35).

[38] ISO Central Secretary. *Rolling bearings — Dynamic load ratings and rating life*. Standard ISO 281:2007. Geneva, CH: International Organization for Standardization, 2016. URL: https://www.iso.org/standard/38102.html (cit. on p. 36).

[39] ISO Central Secretary. *Geometrical product specifications (GPS) — ISO code system for tolerances on linear sizes — Part 2: Tables of standard tolerance classes and limit deviations for holes and shafts*. Standard ISO 286-2:2010. Geneva, CH: International Organization for Standardization, 2010. URL: https://www.iso.org/obp/ui/fr/#iso:std:iso:286:-2:ed-2:v1:en (cit. on p. 37).

[40] *VM108-2P30 datasheet*. Geeplus. URL: https://www.geeplus.com/wp-content/uploads/2019/08/Voice_Coil_motor_VM108-2P30.pdf (cit. on p. 41).

[41] P Wilson and A.H. Mantooth. *Model-Based Engineering for Complex Electronic Systems*. 2013 (cit. on p. 45).

[42] N. S. Nise. *Control System Engineering, 5th ed.* Wiley, 2008. ISBN: 9780470547564 (cit. on p. 52).

[43] Ramsey Faragher. «Understanding the Basis of the Kalman Filter Via a Simple and Intuitive Derivation [Lecture Notes]». In: *IEEE Signal Processing Magazine* 29.5 (2012), pp. 128–132. DOI: 10.1109/MSP.2012.2203621 (cit. on p. 55).

[44] JZ Sasiadek and P Hartana. «Sensor data fusion using Kalman filter». In: *Proceedings of the Third International Conference on Information Fusion*. Vol. 2. IEEE. 2000, WED5–19 (cit. on p. 56).

[45] Andrea Tonoli et al. «Fall identification in rock climbing using wearable device». In: *Proceedings of the Institution of Mechanical Engineers, Part P: Journal of Sports Engineering and Technology* 230.3 (2016), pp. 171–179. DOI: 10.1177/1754337115592749. URL: https://doi.org/10.1177/1754337115592749 (cit. on p. 56).

[46] Y. Bar-Shalom, Xiaorong Li, and T. Kirubarajan. «Estimation with Applications to Tracking and Navigation: Theory, Algorithms and Software». In: 2001 (cit. on p. 56).

[47] J Rawlings and D.Q. Mayne. *Model Predictive Control: Theory and Design*. Jan. 2009 (cit. on p. 59).

[48] *LaunchPad™ developer kit datasheet*. Texas Instruments. URL: `https://www.ti.com/microcontrollers-mcus-processors/microcontrollers/c2000-real-time-control-mcus/design-development.html?utm_source=google&utm_medium=cpc&utm_campaign=epd-c2x-null-C2X_launchpad-cpc-pp-google-eu&utm_content=C2X_launchpad&ds_k=ti+c2000+launchpad&DCM=yes&gclid=Cj0KCQjwxJqHBhC4ARIsAChq4aumr8dXEFkVzovTAvzbLe6FZa7UD6oRZkOECr8CrJmpntNQmhANgr0aAiUfEALw_wcB&gclsrc=aw.ds` (cit. on p. 59).

[49] *65-V max 3-phase smart gate driver with current shunt amplifiers*. Texas Instruments. URL: `https://www.ti.com/product/DRV8323?dcm=yes&utm_source=google&utm_medium=cpc&utm_campaign=asc-mdbu-null-prodfolderdynamic-cpc-pf-google-wwe&utm_content=prodfolddynamic&ds_k=DYNAMIC+SEARCH+ADS&DCM=yes&gclsrc=aw.ds&gclid=Cj0KCQjwxJqHBhC4ARIsAChq4avwkam5lrLHDfsam5PJQ1UmSynYzhj3hpS46Mkn8yUm5aCUDRiPE1MaAl9nEALw_wcB&gclsrc=aw.ds` (cit. on p. 59).

[50] Andrea Tonoli et al. «A solution for the stabilization of electrodynamic bearings: Modeling and experimental validation». In: *Journal of vibration and acoustics* 133.2 (2011).

[51] TS Indraneel et al. «Levitation array testing for Hyperloop pod design». In: *AIAA Scitech 2019 Forum*. 2019, p. 0787.

[52] Le Sun et al. «A Linear Position Measurement Scheme for Long-Distance and High-Speed Applications». In: *IEEE Transactions on Industrial Electronics* 68.5 (2021), pp. 4435–4447. DOI: `10.1109/TIE.2020.2984447`.

[53] HITOSHI TSUNASHIMA and MASATO ABE. «Static and Dynamic Performance of Permanent Magnet Suspension for Maglev Transport Vehicle». In: *Vehicle System Dynamics* 29.2 (1998), pp. 83–111. DOI: `10.1080/00423119808969368`. URL: `https://doi.org/10.1080/00423119808969368`.

[54] Ove F Storset and Brad Paden. «Infinite dimensional models for perforated track electrodynamic magnetic levitation». In: *Proceedings of the 41st IEEE Conference on Decision and Control, 2002.* Vol. 1. IEEE. 2002, pp. 842–847.

[55] Ruiyang Wang and Bingen Yang. «Transient Response of Inductrack Systems for Maglev Transport: Part I—A New Transient Model». In: *Journal of Vibration and Acoustics* 142.3 (2020), p. 031005.

[56] *7206-BECBP angular contact ball bearings*. SKF group.

[57] Shu-Li Sun and Zi-Li Deng. «Multi-sensor optimal information fusion Kalman filter». In: *Automatica* 40.6 (2004), pp. 1017–1023.

[58] Eric Foxlin. «Inertial head-tracker sensor fusion by a complementary separate-bias Kalman filter». In: *Proceedings of the IEEE 1996 Virtual Reality Annual International Symposium*. IEEE. 1996, pp. 185–194.